A frictional sliding algorithm for liquid droplets

Roger A. Sauer [1]

Aachen Institute for Advanced Study in Computational Engineering Science (AICES), RWTH Aachen University, Templergraben 55, 52056 Aachen, Germany

Published[2] in *Computational Mechanics*, DOI: 10.1007/s00466-016-1324-9
Submitted on 16. April 2016, Revised on 8. August 2016, Accepted on 8. August 2016

Abstract

This work presents a new frictional sliding algorithm for liquid menisci in contact with solid substrates. In contrast to solid-solid contact, the liquid-solid contact behavior is governed by the contact line, where a contact angle forms and undergoes hysteresis. The new algorithm admits arbitrary meniscus shapes and arbitrary substrate roughness, heterogeneity and compliance. It is discussed and analyzed in the context of droplet contact, but it also applies to liquid films and solids with surface tension. The droplet is modeled as a stabilized membrane enclosing an incompressible medium. The contact formulation is considered rate-independent such that hydrostatic conditions apply. Three distinct contact algorithms are needed to describe the cases of frictionless surface contact, frictionless line contact and frictional line contact. For the latter, a predictor-corrector algorithm is proposed in order to enforce the contact conditions at the contact line and thus distinguish between the cases of advancing, pinning and receding. The algorithms are discretized within a monolithic finite element formulation. Several numerical examples are presented to illustrate the numerical and physical behavior of sliding droplets.

Keywords: computational contact mechanics, contact angle hysteresis, liquid meniscus, nonlinear finite element methods, rough surface contact, wetting.

1 Introduction

Liquid droplets are everyday objects with rich mechanical behavior. They undergo large shape changes, they split and coalesce, and they can adhere to vertical walls and ceilings. Apart from scientific study, they are of interest in technological applications. In many of those the droplet interacts with a solid substrate. Examples are spray coating, self-cleaning surface mechanisms, or the use of droplets as transport vehicles. In order to better understand the interaction between liquid droplets and solid substrates, general contact models are required. Those need to be capable of describing the three-dimensional droplet deformation during sticking and sliding contact, which is governed by the complex motion of the contact line as it changes between sticking and sliding contact and thus leads to hysteresis. None of the current droplet contact models achieve the generality and flexibility of the computational formulations that have been developed in the past for solid-solid contact. This work aims at providing such a formulation for liquid-solid contact.

The present focus is on surface-based finite element (FE) discretization methods. The work of Brown et al. (1980) seems to be the first such FE formulation for liquid droplets. It solves

[1] corresponding author, email: sauer@aices.rwth-aachen.de
[2] This pdf is the personal version of an article whose final publication is available at http://link.springer.com

the weak form of the Young-Laplace equation w.r.t. a spherical reference surface. The authors consider the contact line to be pinned and treated as a Dirichlet boundary condition. The formulation has been used subsequently by Lawal and Brown (1982a,b) to study pinned pendant and sessile droplets. In later work, discretization techniques were presented that minimize the free energy in the system, which is essentially equivalent to solving the weak form of the Young-Laplace equation. Such approaches were considered by Rotenberg et al. (1984); Brakke (1992) and Iliev (1995). The latter work was extended by Iliev and Pesheva (2006) to consider more general conditions at the contact line, including arbitrary contact angles and rough substrate surfaces, although, the location of the contact line is still prescribed. The *Surface Evolver* (SE) software provided by Brakke (1992) has become a popular tool used by many other researchers. Among those, Santos and White (2011) developed a hysteretic contact line algorithm on flat surfaces for the SE based on a trial movement of the contact line. The approach seems to be similar to the earlier work of Park and Jacobi (2009), which unfortunately did not provide any details of the numerical formulation. Hysteresis in the framework of SE is also considered by Chou et al. (2012), but also there no numerical details are given. Also Prabhala et al. (2013) present a method to incorporate contact angle hysteresis into SE, and use it to analyze pendant and coalescing droplets. Later, also sessile drops were analysed (Janardan and Panchagnula, 2014). Another hysteresis formulation for SE was considered by Semprebon and Brinkmann (2014) in order to study the transition from pinning to steady state sliding.

In the above formulations, the conditions at the contact line are prescribed as boundary conditions instead of enforcing contact constraints. These conditions are then solved in a staggered manner instead of formulating monolithic schemes as they are usually considered for solid-solid contact. Also, most of the above discretization methods are not very general and are restricted to special deformations (e.g. based on spherical coordinates) or special constitutive behavior (e.g. restricted to constant surface tension). Further, the discretization is often based on triangular meshes.

The present work considers a very general FE framework that admits arbitrary deformations and material models, and can be used in conjunction with arbitrary finite element meshes. Contact is described by contact constraints on the contact surface and contact line. The formulation is fully implicit and solved monolithically. It is based on the FE model of Sauer (2014), which in turn is based on the membrane theory of Steigmann (1999) and the corresponding FE formulation of Sauer et al. (2014). In Sauer (2014) the contact angle was considered fixed, with no hysteresis occurring. Hysteresis is now considered here, formulating a friction algorithm based on the general framework of computational contact mechanics (Laursen, 2002; Wriggers, 2006) that admits general substrate topography, heterogeneity and compliance. The current formulation is restricted to non-deforming substrates, however, the formulation is suitable for the extension to deforming substrates. In that case, the challenge lies in the description of the wetting ridge that moves across the substrate surface during sliding. Only if the droplet is pinned, the case is rather simple and can been treated without considering a contact algorithm (Sauer, 2016). The friction algorithm proposed here is conceptionally similar to the algorithms considered by Santos and White (2011) and Prabhala et al. (2013), although those are staggered approaches that are formulated for flat surfaces, while here no such restrictions apply. The following list summarizes the novelties of this work:

- A new and general sliding algorithm is formulated for liquid menisci.
- It is solved within a general nonlinear FE surface formulation.
- The solution scheme is fully implicit and monolithic – no staggering is used.
- Arbitrary meniscus shapes and substrate roughness can be considered.

- Locally varying contact angles can be considered.

Apart from FE models based on an explicit surface discretization also other solution methods for contact angle hysteresis have been considered in the past, such as analytical methods (Dussan V. and Chow, 1983), finite difference methods (Milinazzo and Shinbrot, 1988), molecular dynamics (Thompson and Robbins, 1989), spectral boundary elements (Dimitrakopoulos and Higdon, 1999), level set methods (Sethian and Smerekar, 2003), approximation by circles (ElSherbini and Jacobi, 2004), Lattice-Boltzmann methods (Dupuis and Yeomans, 2006), density functional theory (Berim and Ruckenstein, 2008), volume of fluid methods (Fang et al., 2008), meshless methods (Das and Das, 2009), embedded surface methods (Dong, 2012) and volumetric FE (Minaki and Li, 2014). For a recent review of the treatment of dynamic contact lines in flow problems see Sui et al. (2014).

The remainder of this paper is structured as follows: Sec. 2 gives a summary of the hydrostatic droplet equations. The contact characteristics of liquid-solid interfaces are then discussed in Sec. 3, while Sec. 4 provides the algorithmic treatment of liquid-solid contact. This distinguishes between frictionless surface contact (Sec. 4.1), frictionless line contact (Sec. 4.2) and frictional line contact (Sec. 4.3). Sec. 5 then presents the finite element discretization of the droplet equations. In Sec. 6 four numerical examples are considered to illustrate the proposed computational model. The paper concludes with Sec. 7.

2 Liquid membranes

This section gives a brief summary of the governing equations for hydrostatic droplets following Sauer (2014). In general, the droplet surface $\mathcal{S}$ can be described by the mapping

$$\boldsymbol{x} = \boldsymbol{x}(\xi^\alpha) \ , \tag{1}$$

where ξ^α (with $\alpha = 1, 2$) are curvilinear surface coordinates. From this the tangent vectors $\boldsymbol{a}_\alpha := \partial \boldsymbol{x}/\partial \xi^\alpha$, the surface metric $a_{\alpha\beta} := \boldsymbol{a}_\alpha \cdot \boldsymbol{a}_\beta$, its inverse $[a^{\alpha\beta}] := [a_{\alpha\beta}]^{-1}$, the dual tangent vectors $\boldsymbol{a}^\alpha := a^{\alpha\beta}\, \boldsymbol{a}_\beta$, the surface identity tensor $\boldsymbol{i} := \boldsymbol{a}_\alpha \otimes \boldsymbol{a}^\alpha = \boldsymbol{a}^\alpha \otimes \boldsymbol{a}_\alpha$ and the surface normal $\boldsymbol{n} := \boldsymbol{a}_1 \times \boldsymbol{a}_2 / \|\boldsymbol{a}_1 \times \boldsymbol{a}_2\|$ can be defined.[3] Mapping (1) is the solution of the general field equation

$$(\boldsymbol{\sigma} \boldsymbol{a}^\alpha)_{;\alpha} + \boldsymbol{f} = \boldsymbol{0} \tag{2}$$

and the boundary conditions

$$\begin{aligned} \boldsymbol{x} &= \bar{\boldsymbol{x}} \quad \text{on } \partial_x \mathcal{S} \ , \\ \boldsymbol{\sigma} \boldsymbol{m} = \boldsymbol{t} &= \bar{\boldsymbol{t}} \quad \text{on } \partial_u \mathcal{S} \ , \end{aligned} \tag{3}$$

on the deformation and traction field at the surface boundary $\partial \mathcal{S}$ with outward unit normal $\boldsymbol{m}$. Here, $(...)_{;\alpha}$ denotes the co-variant derivative w.r.t. ξ^α. For liquid membranes the surface stress tensor is given by

$$\boldsymbol{\sigma} = \gamma\, \boldsymbol{i} \ , \tag{4}$$

where γ is the surface tension. γ is a scalar that is analogous to the pressure in classical, 3D fluid mechanics. Since constitutive relation (4) offers no resistance to in-plane shearing, the formulation needs to be stabilized. A very accurate approach is to split field equation (2) into in-plane and out-of-plane contributions and add a numerical stabilization stress to the in-plane equation while leaving the out-of-plane equation alone (Sauer, 2014). In this case, the corresponding weak form is given by

$$G := G_{\text{int}} + G_{\text{c}} - G_{\text{f}} - G_{\text{ext}} = 0 \quad \forall\ \boldsymbol{w} \in \mathcal{W} \ , \tag{5}$$

[3] Here and in the following, all vectors and tensors are written in bold font.

with the virtual work contributions

$$\begin{aligned} G_{\text{int}} &:= \int_{\mathcal{S}} \gamma\, \boldsymbol{w}_{;\alpha} \cdot \boldsymbol{a}^{\alpha}\, \mathrm{d}a + \int_{\mathcal{S}} w_{\alpha;\beta}\, \sigma_{\text{sta}}^{\alpha\beta}\, \mathrm{d}a \;, \\ G_{\text{c}} &:= -\int_{\mathcal{S}} \boldsymbol{w} \cdot \boldsymbol{f}_{\text{c}}\, \mathrm{d}a \;, \\ G_{\text{f}} &:= \int_{\mathcal{S}} \boldsymbol{w} \cdot \boldsymbol{f}_{\text{f}}\, \mathrm{d}a \;, \\ G_{\text{ext}} &:= \int_{\mathcal{S}} \boldsymbol{w} \cdot \bar{\boldsymbol{f}}\, \mathrm{d}a + \int_{\partial_t \mathcal{S}} \boldsymbol{w} \cdot \bar{\boldsymbol{t}}\, \mathrm{d}s + \int_{\mathcal{C}} \boldsymbol{w} \cdot \boldsymbol{q}_{\text{c}}\, \mathrm{d}s \;. \end{aligned} \tag{6}$$

Here $\boldsymbol{w} = w_\alpha\, \boldsymbol{a}^\alpha + w\, \boldsymbol{n}$ is a kinematically admissible variation of the deformation, $\boldsymbol{f}_{\text{c}}$ and $\boldsymbol{q}_{\text{c}}$ are surface and line contact tractions, $\boldsymbol{f}_{\text{f}}$ are fluid tractions, and $\bar{\boldsymbol{f}}$ and $\bar{\boldsymbol{t}}$ are external loads; $\sigma_{\text{sta}}^{\alpha\beta}$ denotes the components of the stabilization stress. The two choices (Sauer, 2014)

$$\sigma_{\text{sta}}^{\alpha\beta} = \mu / J \big(A^{\alpha\beta} - a^{\alpha\beta} \big) \;, \tag{7}$$

based on numerical stiffness, and

$$\sigma_{\text{sta}}^{\alpha\beta} = \mu / J \big(a_{\text{pre}}^{\alpha\beta} - a^{\alpha\beta} \big) \;, \tag{8}$$

based on numerical viscosity, are considered here. Here $A^{\alpha\beta}$ and $a_{\text{pre}}^{\alpha\beta}$ characterize the surface stretch in the reference configuration and at the preceding load step; μ is a stabilization parameter. Eq. (8) can be derived from physical viscosity (Sauer et al., 2016).

For hydrostatic fluid behavior, the physical terms in the weak form can be derived from a global potential (Sauer, 2016). In this case $\boldsymbol{f}_{\text{f}} = p_{\text{f}}\, \boldsymbol{n}$, $\bar{\boldsymbol{f}} = -\bar{p}\, \boldsymbol{n}$ and $\boldsymbol{f}_{\text{c}} = -p_{\text{c}}\, \boldsymbol{n}$, where p_{f} is the fluid pressure within the droplet and $\bar{p}$ and p_{c} are external pressures due to the surrounding environment and contact. The former is given by

$$p_{\text{f}} = p_{\text{v}} + \rho\, \boldsymbol{g} \cdot \boldsymbol{x} \;, \tag{9}$$

where $\boldsymbol{g}$ is the gravity vector and p_{v} is the capillary pressure. If the interior droplet medium is considered incompressible, p_{v} corresponds to the Lagrange multiplier of the volume constraint

$$g_{\text{v}} = V_0 - V = 0 \;. \tag{10}$$

The contact pressure p_{c} and contact line load $\boldsymbol{q}_{\text{c}}$ are discussed in the following two sections.

Remark 1: Field equation (2) admits more complex material models than model (4). Stretch-related stresses and even bending-related stresses can be considered. Examples are given in Sauer and Duong (2015). It is further noted that the above formulation does not consider a line tension along $\mathcal{C}$, although also this can be incorporated into the formulation, e.g. see Steigmann and Li (1995).

3 Liquid-solid contact characteristics

This section discusses the contact characteristics of liquid-solid interfaces by looking at liquid droplets. Both static and dynamic droplets are discussed. It is seen that the contact behavior of liquids exhibits some properties that are uncommon for solids.
A liquid droplet $\mathcal{D}$ sitting on a solid substrate $\mathcal{B}$ forms a distinct contact angle at the triple line $\mathcal{C}$, where the solid-liquid, liquid-gas and solid-gas interfaces $\mathcal{S}_{\text{SL}}$, $\mathcal{S}_{\text{LG}}$ and $\mathcal{S}_{\text{SG}}$ meet, see Fig. 1a.

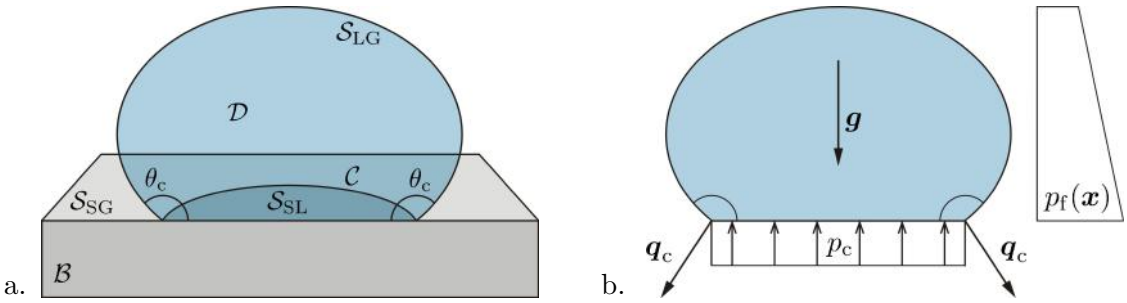

Figure 1: Liquid-solid contact characteristics: (a) contact angle θ_{c} at the triple line $\mathcal{C}$; (b) contact forces for hydrostatic conditions.

3.1 Static droplets

In the quasi-static case, the contact forces on $\mathcal{S}_{\mathrm{SL}}$ and $\mathcal{C}$ are simple to determine: The contact pressure p_{c} on $\mathcal{S}_{\mathrm{SL}}$ is uniform and equal to the hydrostatic fluid pressure, see Fig. 1b. The line load $\boldsymbol{q}_{\mathrm{c}}$ at the triple line $\mathcal{C}$ follows directly from the contact angle and the surface tensions of the three interfaces (see Sec. 4.2). This line load is balanced by a corresponding line load acting on the substrate. Due to the singular nature of this line load, a wetting ridge will form on the substrate (Sauer, 2016). For very stiff substrates, the wetting ridge is very small and may be neglected.

When formulating a free body diagram of the liquid droplet a general question arises: Where to place interface $\mathcal{S}_{\mathrm{SL}}$ (along with its physical properties) – on the droplet or on the substrate side? This leads to the two modeling paradigms shown in Fig. 2. In the computational modeling

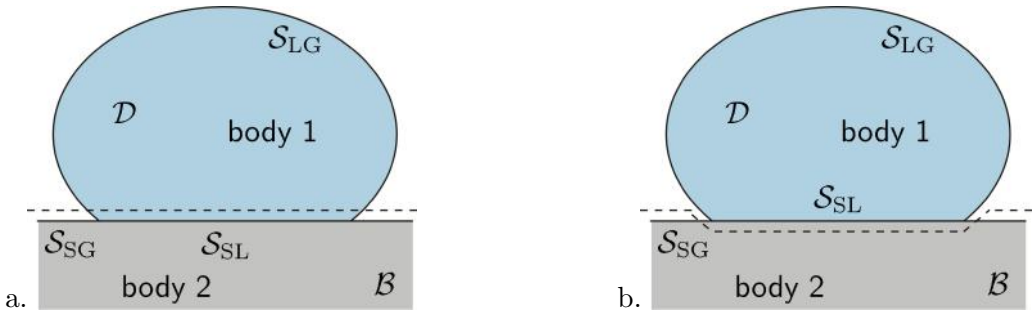

Figure 2: Liquid-solid contact paradigms: (a) *open droplet contact model* (body 1: $\mathcal{D} \cup \mathcal{S}_{\mathrm{LG}}$, body 2: $\mathcal{B} \cup \mathcal{S}_{\mathrm{SG}} \cup \mathcal{S}_{\mathrm{SL}}$); (b) *closed droplet contact model* (body 1: $\mathcal{D} \cup \mathcal{S}_{\mathrm{LG}} \cup \mathcal{S}_{\mathrm{SL}}$, body 2: $\mathcal{B} \cup \mathcal{S}_{\mathrm{SG}}$).

considered here, the *closed droplet contact model* – where $\mathcal{S}_{\mathrm{SL}}$ is accounted for on the droplet side – is used (Fig. 2b). As long as the surface tension within $\mathcal{S}_{\mathrm{SL}}$ is constant, it is easy to exchange the two models as they will only differ in the way $\boldsymbol{q}_{\mathrm{c}}$ is defined. Note that this issue usually does not arise in solids, since the surface tension is neglected and consequently $\boldsymbol{q}_{\mathrm{c}} = \boldsymbol{0}$. However, if surface tensions are accounted for in solids, the contact modeling discussed here, equally applies.

Fig. 1b shows that in the hydrostatic case, tangential contact forces can only be transferred at the triple line through $\boldsymbol{q}_{\mathrm{c}}$. In this case, we require three different contact algorithms: One for frictionless surface contact, one for frictionless line contact and one for frictional line contact.

These three cases are discussed in Sec. 4.

3.2 Moving droplets: sliding vs. rolling

If the substrate surface is inclined, the droplet deforms laterally and may start moving. The droplet motion can be characterized by rolling, by sliding or by a mixture of both. A droplet that is almost spherical can be expected to roll, just like a solid sphere would. Droplets are almost spherical if gravity is negligible and $\theta_c \to 180°$. For droplets that are not spherical, the question whether sliding or rolling motion dominates depends on the droplet-substrate interface. If the fluid particles stick to the substrate (corresponding to a no-slip boundary condition), the droplet can be expected to roll. For flat droplets, this motion is also referred to as *tank-treading*. If the fluid particles slide on the substrate, two further cases need to be distinguished: frictionless sliding and frictional sliding. The first case (which corresponding to a zero shear traction boundary condition) leads to a pure sliding motion of the droplet. The second case leads to mixed rolling and sliding motion. The parameters that lead to rolling or sliding dominated motion have been investigated extensively in the literature, e.g. see Thampi et al. (2013) and references therein.
In this work, the focus is on the computational modeling of sliding, since this case has not received much attention in the past. As discussed above, sliding can be expected to be the dominating case for flat droplets on smooth substrates. Sliding droplets require an algorithm for contact angle hysteresis, which is the major novelty of this work. During (pure) sliding, the fluid within the droplet does not rotate, so that there is no need to numerically solve for the flow field. Therefore hydrostatic conditions can still be considered. Rolling on the other hand, leads to rotating fluid flow that in general needs to be determined computationally. The case of rolling is outside the present scope of study.

4 Contact description of liquids

This section provides general contact algorithms for the three cases of frictionless surface contact, frictionless line contact and frictional line contact. The first two cases are summarized from Sauer (2014).

4.1 Surface contact

The surface contact of liquids can be treated in the same fashion as for solids, and in principle any contact algorithm can be used. Generally, those enforce the impenetrability constraint

$$g_n = (\boldsymbol{x}_c - \boldsymbol{x}_p) \cdot \boldsymbol{n}_p \geq 0 \quad \forall\, \boldsymbol{x}_c \in \mathcal{S} \;, \tag{11}$$

between the two bodies. Here $\boldsymbol{x}_c \in \mathcal{S}_{SL}$ is an arbitrary point on the contact surface of the droplet and $\boldsymbol{x}_p \in \partial\mathcal{B}$ is its corresponding neighbor on the substrate surface; $\boldsymbol{n}_p$ denotes the surface normal at $\boldsymbol{x}_p$. Point $\boldsymbol{x}_p$ is commonly obtained from a closest point projection of $\boldsymbol{x}_c$ onto $\partial\mathcal{B}$, i.e. by solving

$$(\boldsymbol{x}_p - \boldsymbol{x}_c) \cdot \boldsymbol{a}_\alpha^p = 0 \;, \quad \alpha = 1, 2, \tag{12}$$

for the parametric coordinates ξ_p^α defining the projection point from $\boldsymbol{x}_p = \boldsymbol{x}(\xi_p^\alpha)$. Here, $\boldsymbol{a}_\alpha^p$ denote the tangent vectors of $\partial\mathcal{B}$ at $\boldsymbol{x}_p$. During general sliding motion, the projection point

moves across the surface $\partial\mathcal{B}$ (such that $\dot{\xi}_{\mathrm{p}}^{\alpha} \neq 0$) and needs to be recomputed at each new time step. From time t_n to t_{n+1}, $\xi_{\mathrm{p}}^{\alpha}$ thus updates by

$$\xi_{\mathrm{p}\,n+1}^{\alpha} = \xi_{\mathrm{p}\,n}^{\alpha} + \Delta\xi_{\mathrm{p}\,n+1}^{\alpha} \ . \tag{13}$$

In Sauer (2014) a simple penalty formulation is considered to enforce (11). This results in the contact pressure

$$p_{\mathrm{c}} = \begin{cases} -\epsilon_{\mathrm{n}}\, g_{\mathrm{n}} & \text{if } g_{\mathrm{n}} < 0 \ , \\ 0 & \text{if } g_{\mathrm{n}} \geq 0 \ , \end{cases} \tag{14}$$

where ϵ_{n} is the chosen penalty parameter. Fig. 3 shows an example taken from Sauer (2014) considering $\boldsymbol{q}_{\mathrm{c}} = \boldsymbol{0}$.

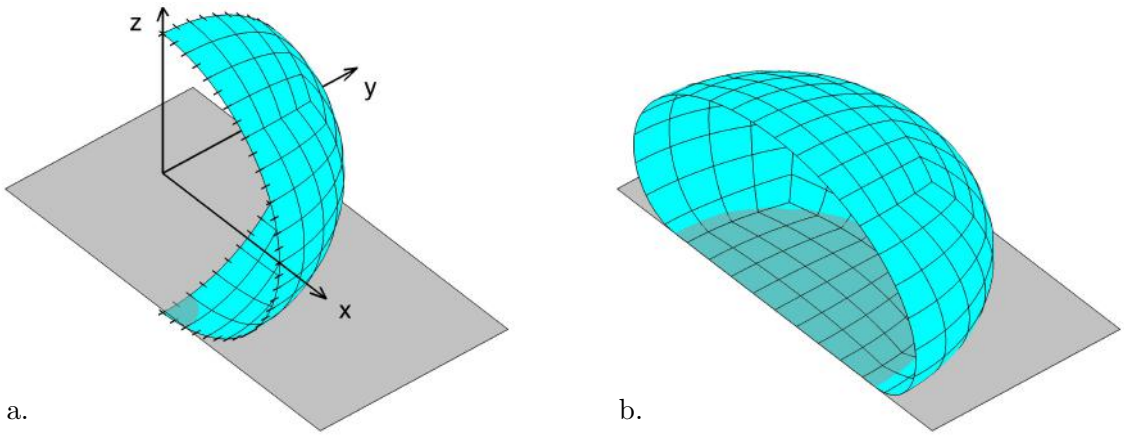

a. b.

Figure 3: Droplet surface contact for $\theta_{\mathrm{c}} = 180°$ (Sauer, 2014): (a) initial configuration with boundary and symmetry conditions, considering $n_{\mathrm{el}} = 96$ quadratic Lagrange FE; (b) deformed configuration for gravity loading with $\rho g = 2\gamma/R_0^2$, where R_0 is the initial droplet radius.

4.2 Frictionless line contact

If $\boldsymbol{q}_{\mathrm{c}} \neq \boldsymbol{0}$, a line contact algorithm is needed. We first summarize the frictionless case already treated in Sauer (2014). According to the *closed droplet contact model*, the line force $\boldsymbol{q}_{\mathrm{c}}$ balances the surface tension of interfaces $\mathcal{S}_{\mathrm{SL}}$ and $\mathcal{S}_{\mathrm{LG}}$ at the triple line $\mathcal{C}$ as is shown in Fig. 4. According to the figure, the forces pulling on $\mathcal{C}$ thus are $\boldsymbol{q}_{\mathrm{c}}^0$, $\gamma_{\mathrm{LG}}\,(\sin\theta_{\mathrm{c}}^0\,\boldsymbol{n}_{\mathrm{c}} - \cos\theta_{\mathrm{c}}^0\,\boldsymbol{m}_{\mathrm{c}})$ and $-\gamma_{\mathrm{SL}}\boldsymbol{m}_{\mathrm{c}}$, such that

$$\boldsymbol{q}_{\mathrm{c}} = q_{\mathrm{m}}\,\boldsymbol{m}_{\mathrm{c}} + q_{\mathrm{n}}\,\boldsymbol{n}_{\mathrm{c}} \ , \tag{15}$$

where

$$\begin{aligned} q_{\mathrm{m}} &= \gamma_{\mathrm{SL}} + \gamma_{\mathrm{LG}}\cos\theta_{\mathrm{c}} \ , \\ q_{\mathrm{n}} &= \quad - \gamma_{\mathrm{LG}}\sin\theta_{\mathrm{c}} \ , \end{aligned} \tag{16}$$

for $\theta_{\mathrm{c}} = \theta_{\mathrm{c}}^0$ and $\boldsymbol{q}_{\mathrm{c}} = \boldsymbol{q}_{\mathrm{c}}^0$. Superscript '0' is added to indicate that Fig. 4 characterizes the frictionless case. In that case $q_{\mathrm{m}} = \gamma_{\mathrm{SG}}$ and Eq. (16.1) becomes Young's equation, which characterizes the tangential force balance at $\mathcal{C}$. Vectors $\boldsymbol{n}_{\mathrm{c}}$ and $\boldsymbol{m}_{\mathrm{c}}$ are perpendicular unit vectors that are normal to the contact line $\mathcal{C}$ as shown in Fig. 4. The surface normal $\boldsymbol{n}_{\mathrm{c}}$ is defined from the substrate orientation, while $\boldsymbol{m}_{\mathrm{c}}$ can be computed from

$$\boldsymbol{m}_{\mathrm{c}} = \frac{\boldsymbol{a}_{\mathrm{c}} \times \boldsymbol{n}_{\mathrm{c}}}{\|\boldsymbol{a}_{\mathrm{c}} \times \boldsymbol{n}_{\mathrm{c}}\|} \ , \tag{17}$$

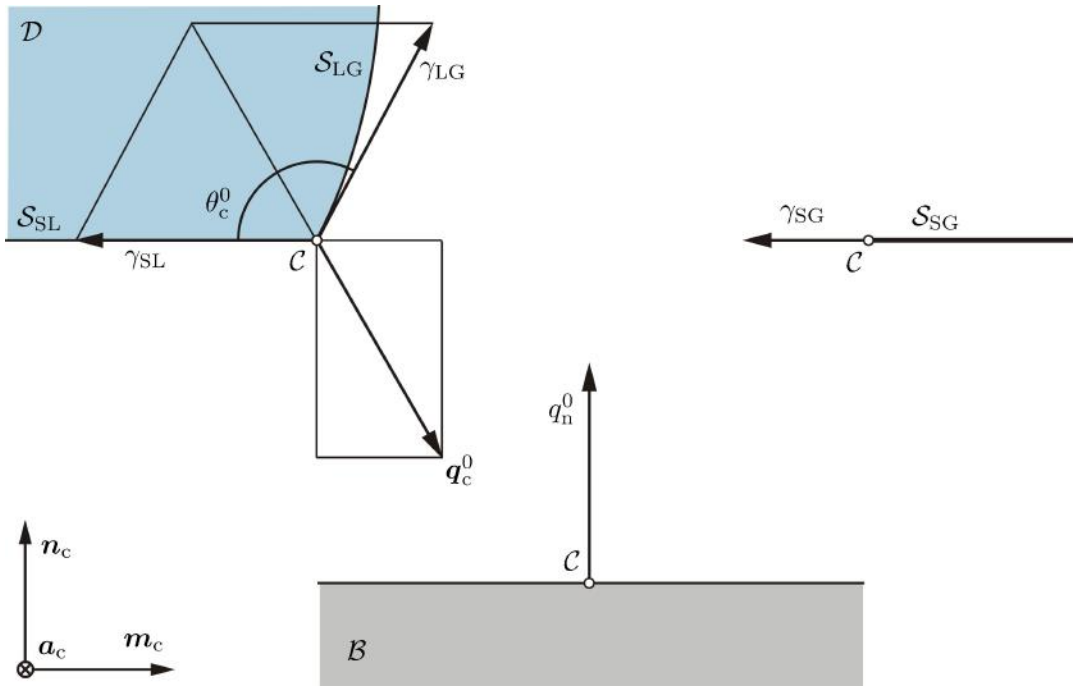

Figure 4: Frictionless line contact: Equilibrium at the contact line $\mathcal{C}$ within the plane perpendicular to $\mathcal{C}$. Shown is a free body diagram of the three 'bodies' $\mathcal{B}$, $\mathcal{S}_{\mathrm{SG}}$ and $\mathcal{D} \cup \mathcal{S}_{\mathrm{SL}} \cup \mathcal{S}_{\mathrm{LG}}$. Here, $\boldsymbol{q}_{\mathrm{c}}^0$ is a vector, while γ_{SL}, γ_{LG}, γ_{SG} and q_n^0 are vector magnitudes.

where $\boldsymbol{a}_{\mathrm{c}}$ is the tangent vector to $\mathcal{C}$. It is defined in analogy to the surface tangents $\boldsymbol{a}_\alpha$ (see Sec. 2), as $\boldsymbol{a}_{\mathrm{c}} = \partial \boldsymbol{x}_{\mathrm{c}} / \partial \xi$, where $\boldsymbol{x}_{\mathrm{c}} = \boldsymbol{x}_{\mathrm{c}}(\xi)$ is the parameterization of $\mathcal{C}$. Contrary to $\boldsymbol{n}_{\mathrm{c}}$ and $\boldsymbol{m}_{\mathrm{c}}$, $\boldsymbol{a}_{\mathrm{c}}$ is not a unit vector. Therefore $\bar{\boldsymbol{a}}_{\mathrm{c}} = \boldsymbol{a}_{\mathrm{c}} / \|\boldsymbol{a}_{\mathrm{c}}\|$ is introduced.
In Sauer (2014) a straight-forward contact algorithm is proposed for the application of $\boldsymbol{q}_{\mathrm{c}}$, considering arbitrary orientations and curvatures of the substrate surface. Fig. 5 shows the procedure for a simple example. As noted in Sauer (2014), the initial location of $\mathcal{C}$ can be

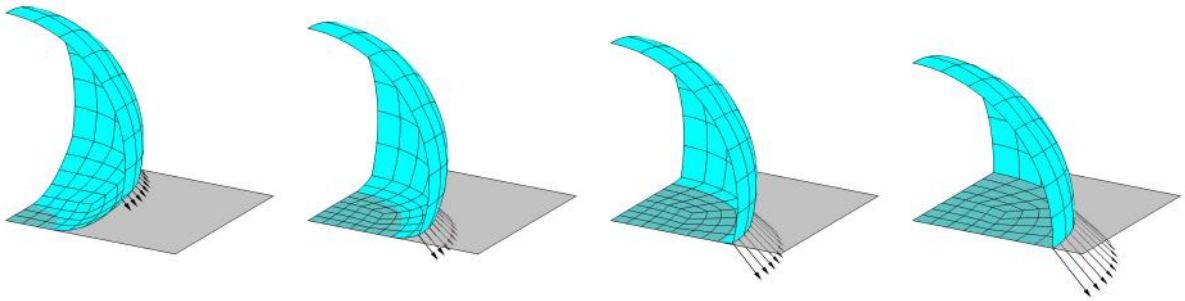

Figure 5: Droplet line contact for $\theta_{\mathrm{c}} = 90°$: Stepwise application of line force $\boldsymbol{q}_{\mathrm{c}}$ (Sauer, 2014). Shown are the intermediate configurations at $\{1/4,\ 1/2,\ 3/4,\ 1\} \times \boldsymbol{q}_{\mathrm{c}}$ (left to right).

chosen arbitrarily due to the absence of shear stiffness in the liquid membrane.

For now, the surface tensions γ_{SG}, γ_{SL} and γ_{LG}, as well as the contact angle θ_{c} have been considered constant. Therefore the net resultant of the entire line load $\boldsymbol{q}_{\mathrm{c}}$ around $\mathcal{C}$ has no tangential component and hence no frictional forces can be transmitted across the interface. In order to transfer frictional forces, the generalization of Sec. 4.3 is needed.

4.3 Frictional line contact

This section presents a general contact algorithm to describe the frictional contact behavior of liquids. The formulation is similar to solids in the sense that also sticking and sliding states have to be distinguished. But it is quite different in the way these are characterized. The state of sticking – usually denoted as pinning in the case of liquids – is characterized by the tangential sticking constraint

$$\dot{g}_m = 0 \quad \forall\, \boldsymbol{x}_\mathrm{c} \in \mathcal{C} \ , \tag{18}$$

where $\dot{g}_m$ denotes the velocity of the contact line along $\boldsymbol{m}_\mathrm{c}$, relative to the substrate motion. This relative velocity is given as

$$\dot{g}_m := \dot{\xi}_\mathrm{p}^\alpha \, \boldsymbol{a}_\alpha^\mathrm{p} \cdot \boldsymbol{m}_\mathrm{c} \ , \tag{19}$$

based on the quantities introduced in Secs. 4.1 and 4.2. The physical motion of the contact line along its tangent direction $\bar{\boldsymbol{a}}_\mathrm{c}$ is not restricted.[4] On an abstract level, this setting can be idealized by a microscopic wheel that is aligned along $\bar{\boldsymbol{a}}_\mathrm{c}$ and only resists motion along $\boldsymbol{m}_\mathrm{c}$, see Goyal et al. (1991).
Sticking is further characterized by a limit on the contact angle θ_c, given as

$$0 \leq \theta_\mathrm{r} \leq \theta_\mathrm{c} \leq \theta_\mathrm{a} \leq \pi \ , \tag{20}$$

where θ_a and θ_r are material constants. If the limit values are reached, the contact line begins to slide, either with $\theta_\mathrm{c} = \theta_\mathrm{a}$ (contact line advancing) or with $\theta_\mathrm{c} = \theta_\mathrm{r}$ (contact line receding). Eq. (20) implies

$$-1 \leq \cos\theta_\mathrm{a} \leq \cos\theta_\mathrm{c} \leq \cos\theta_\mathrm{r} \leq 1 \ . \tag{21}$$

Since θ_c is related to the three surface tensions γ_SG, γ_SL and γ_LG, Eq. (21) can also be interpreted as a limit on those γ's. But the γ's are not required to change during pinning – it is sufficient to only let the contact angle θ_c change. For simplicity we will thus consider all γ's to be fixed.

Remark 2: If the γ's do change, a model is needed for that, e.g. an elastic membrane model for the surface stresses γ_SL and γ_SG, possibly with a yield limit. Such an approach is not considered here. Instead we assume all γ's to be constant, and the hysteresis to come solely from θ_c.

Multiplying (21) by $-\gamma_\mathrm{LG}$ and adding $\gamma_\mathrm{SG} - \gamma_\mathrm{SL}$ yields the relation

$$\gamma_\mathrm{r} \leq t_\mathrm{t} \leq \gamma_\mathrm{a} \ , \tag{22}$$

where

$$\begin{aligned} \gamma_\mathrm{a} &:= \gamma_\mathrm{SG} - \gamma_\mathrm{SL} - \gamma_\mathrm{LG}\cos\theta_\mathrm{a} \ , \\ \gamma_\mathrm{r} &:= \gamma_\mathrm{SG} - \gamma_\mathrm{SL} - \gamma_\mathrm{LG}\cos\theta_\mathrm{r} \end{aligned} \tag{23}$$

and

$$t_\mathrm{t} = \gamma_\mathrm{SG} - \gamma_\mathrm{SL} - \gamma_\mathrm{LG}\cos\theta_\mathrm{c} \ . \tag{24}$$

The parameters $\gamma_\mathrm{a} \geq 0$ and $\gamma_\mathrm{r} \leq 0$ can be considered as new material constants. The quantity t_t corresponds to a tangential friction force between the contact line $\mathcal{C}$ and the substrate surface $\partial\mathcal{B}$. It is illustrated in Fig. 6. To be precise, the force $\boldsymbol{t}_\mathrm{t} = t_\mathrm{t}\,\boldsymbol{m}_\mathrm{c}$ pushes on $\partial\mathcal{B}$ while the force $-\boldsymbol{t}_\mathrm{t}$ retains the droplet. For frictionless contact, this force is zero, such that we come back to the setting of Sec. 4.2 and Fig. 4. For frictional contact, t_t lives in the range given by (22). In this formulation, the limit can be understood as a limit on the tangential force, i.e. as a kinetic criterion instead of a kinematic one. It is noted, that the line load $\boldsymbol{q}_\mathrm{c}$ is still given by Eqs. (15)

[4] For some applications, however, one may want to restrict the mesh motion along $\bar{\boldsymbol{a}}_\mathrm{c}$. Then instead of (18), the classical sticking constraint $\dot{\xi}_\mathrm{p}^\alpha = 0$ should be used (Sauer, 2016).

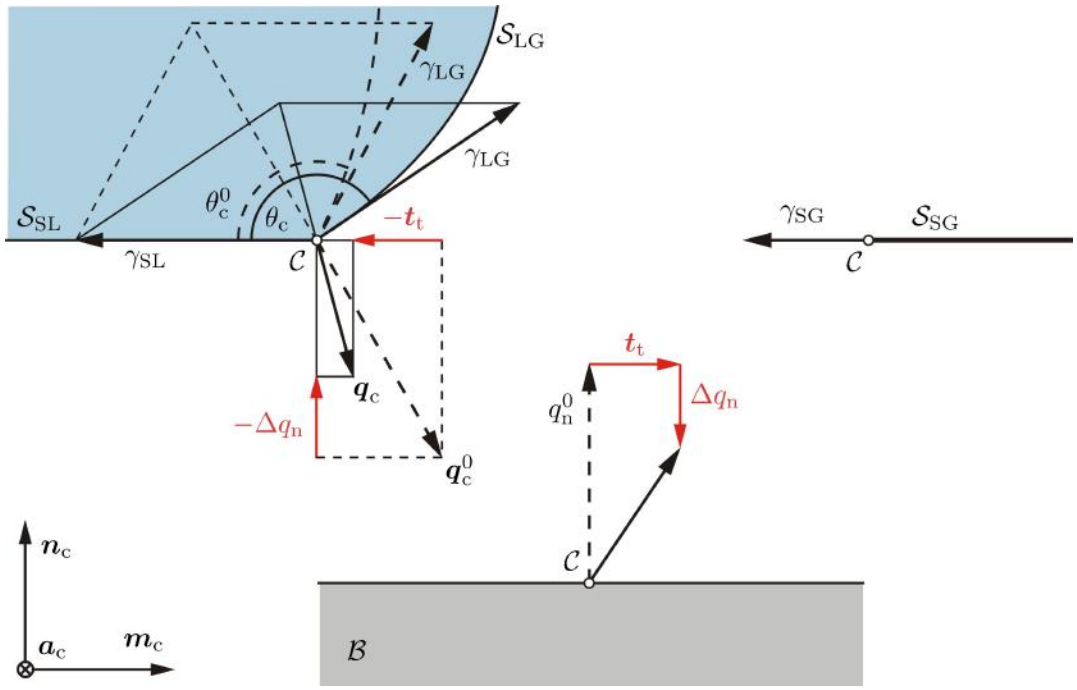

Figure 6: Frictional line contact: Equilibrium at the contact line $\mathcal{C}$, considering θ_{c} to change while the surface tensions γ_{SG}, γ_{SL} and γ_{LG} are considered fixed.

and (16), but now $q_{\mathrm{m}} = \gamma_{\mathrm{SG}} - t_{\mathrm{t}}$. According to Fig. 6, the current contact angle is related to $\boldsymbol{t}_{\mathrm{t}}$ by

$$\theta_{\mathrm{c}} = \arccos\left(\cos\theta_{\mathrm{c}}^0 - \boldsymbol{t}_{\mathrm{t}} \cdot \boldsymbol{m}_{\mathrm{c}}/\gamma_{\mathrm{LG}}\right) . \tag{25}$$

From the two limit states in (22), one can now define the two slip criteria

$$\begin{aligned} f_{\mathrm{a}} &:= \boldsymbol{t}_{\mathrm{t}} \cdot \boldsymbol{m}_{\mathrm{c}} - \gamma_{\mathrm{a}} \leq 0 \ , \\ f_{\mathrm{r}} &:= \boldsymbol{t}_{\mathrm{t}} \cdot \boldsymbol{m}_{\mathrm{c}} - \gamma_{\mathrm{r}} \geq 0 \ . \end{aligned} \tag{26}$$

It then follows that

$$\begin{aligned} f_{\mathrm{a}} < 0 \quad \text{and} \quad f_{\mathrm{r}} > 0 \quad &\Leftrightarrow \quad \text{sticking}, \\ f_{\mathrm{a}} = 0 \quad \text{or} \quad f_{\mathrm{r}} = 0 \quad &\Leftrightarrow \quad \text{sliding}. \end{aligned} \tag{27}$$

Fig. 7 gives an illustration of the feasible regions in t_{t}–space ($t_{\mathrm{t}} = \boldsymbol{t}_{\mathrm{t}} \cdot \boldsymbol{m}_{\mathrm{c}}$). Note that during

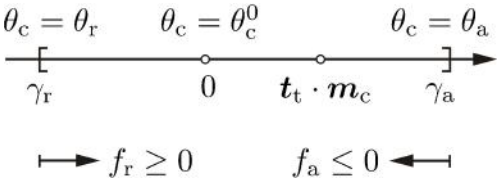

Figure 7: Frictional line contact: feasible traction state at $\mathcal{C}$.

frictional contact, the tangential traction t_{t} can still become zero. To mark this special situation, the corresponding contact angle is denoted by θ_{c}^0.

Remark 3: Alternatively, one can also introduce the slip criteria

$$\begin{aligned} \bar{f}_{\mathrm{a}} &:= f_{\mathrm{a}}/\gamma_{\mathrm{LG}} = \cos\theta_{\mathrm{a}} - \cos\theta_{\mathrm{c}} \leq 0 \ , \\ \bar{f}_{\mathrm{r}} &:= f_{\mathrm{r}}/\gamma_{\mathrm{LG}} = \cos\theta_{\mathrm{r}} - \cos\theta_{\mathrm{c}} \geq 0 \ . \end{aligned} \tag{28}$$

This formulation is used in the alternative algorithm of Remark 8. It avoids using the tangential traction $\boldsymbol{t}_\mathrm{t}$.

Remark 4: The two slip criteria of Eq. (26) can be combined into the single slip criterion

$$f_\mathrm{s} = |\boldsymbol{t}_\mathrm{t} \cdot \boldsymbol{m}_\mathrm{c} - \gamma_0| - \gamma_\mathrm{s} \leq 0 \ , \tag{29}$$

where

$$\begin{aligned} \gamma_0 &:= (\gamma_\mathrm{a} + \gamma_\mathrm{r})/2 \ , \\ \gamma_\mathrm{s} &:= (\gamma_\mathrm{a} - \gamma_\mathrm{r})/2 \ . \end{aligned} \tag{30}$$

In order to enforce conditions (18) and (26), the friction formulation of Sauer and De Lorenzis (2015) is used, considering the framework of Sec. 4.1, now with $\boldsymbol{x}_\mathrm{c} \in \mathcal{C}$. The formulation considers a commonly used penalty regularization of constraint (18), allowing for some tangential motion to occur during sticking. To distinguish this motion from sliding, a split of the total slip into an irreversible sliding motion and a reversible (i.e. elastic) sticking motion is considered (Laursen, 2002; Wriggers, 2006). This split can be formulated on ξ^α_p, so that we have

$$\xi^\alpha_{\mathrm{p}\,n} = \xi^\alpha_{\mathrm{s}\,n} + \Delta\xi^\alpha_{\mathrm{e}\,n} \tag{31}$$

at time step t_n. In the case of solids, the tangential contact traction can then be defined by

$$\boldsymbol{t}^n_\mathrm{t} = \epsilon_\mathrm{t}\big(\boldsymbol{x}^n_\mathrm{m}(\boldsymbol{\xi}^n_\mathrm{p}) - \boldsymbol{x}^n_\mathrm{m}(\boldsymbol{\xi}^n_\mathrm{s})\big) \ , \tag{32}$$

where ϵ_t is the tangential penalty parameter, $\boldsymbol{x}_\mathrm{m}$ dotes a surface point on $\partial\mathcal{B}$ (the designated master surface) and $\boldsymbol{\xi} = (\xi^1, \xi^2)$. In order to determine the friction state at the new time step t_{n+1}, a predictor-corrector algorithm is considered, predicting first a sticking state and then correcting that into a sliding state if appropriate. Based on (32), the prediction step is characterized by the trial traction (Sauer and De Lorenzis, 2015)

$$\boldsymbol{t}^\mathrm{trial}_{\mathrm{t}\,n+1} = \epsilon_\mathrm{t}\big(\boldsymbol{x}^{n+1}_\mathrm{p} - \boldsymbol{x}^{n+1}_\mathrm{m}(\boldsymbol{\xi}^n_\mathrm{s})\big) \ , \tag{33}$$

where $\boldsymbol{x}^{n+1}_\mathrm{p} = \boldsymbol{x}^{n+1}_\mathrm{m}(\boldsymbol{\xi}^{n+1}_\mathrm{p})$. This has to be modified for liquids. Since the liquid membrane supports no shear stress, we need to replace (32) and (33) by

$$\boldsymbol{t}^n_\mathrm{t} = \epsilon_\mathrm{t}\,\big(\boldsymbol{m}^n_\mathrm{c} \otimes \boldsymbol{m}^n_\mathrm{c}\big)\big(\boldsymbol{x}^n_\mathrm{p} - \boldsymbol{x}^n_\mathrm{m}(\boldsymbol{\xi}^n_\mathrm{s})\big) \tag{34}$$

and

$$\boldsymbol{t}^\mathrm{trial}_{\mathrm{t}\,n+1} := \epsilon_\mathrm{t}\,\big(\boldsymbol{m}^{n+1}_\mathrm{c} \otimes \boldsymbol{m}^{n+1}_\mathrm{c}\big)\big(\boldsymbol{x}^{n+1}_\mathrm{p} - \boldsymbol{x}^{n+1}_\mathrm{m}(\boldsymbol{\xi}^n_\mathrm{s})\big) \ . \tag{35}$$

In these expressions we can then simply replace $\boldsymbol{x}_\mathrm{p}$ by $\boldsymbol{x}_\mathrm{c}$, since $\boldsymbol{m}_\mathrm{c} \cdot \boldsymbol{x}_\mathrm{p} = \boldsymbol{m}_\mathrm{c} \cdot \boldsymbol{x}_\mathrm{c}$. Using $\boldsymbol{t}^\mathrm{trial}_\mathrm{t}$ the slip criteria (26) are checked. If either of them is not satisfied, the traction state needs to be mapped back to the feasible region. This return mapping can be derived in analogy to solid contact (Sauer and De Lorenzis, 2015) starting from the evolution law for $\boldsymbol{\xi}_\mathrm{s}$, which for solids is given by

$$\dot{\xi}^\alpha_\mathrm{s} = \lambda\, \boldsymbol{n}_\mathrm{t} \cdot \boldsymbol{a}^\alpha_\mathrm{s} \ , \tag{36}$$

where $\boldsymbol{a}^\alpha_\mathrm{s}$ are the contra-variant tangent vectors of $\partial\mathcal{B}$ at $\boldsymbol{x}_\mathrm{m}(\boldsymbol{\xi}_\mathrm{s})$, λ is a proportionality factor, and $\boldsymbol{n}_\mathrm{t}$ denotes the change of the slip function w.r.t. $\boldsymbol{t}_\mathrm{t}$. In the case of liquids this is

$$\boldsymbol{n}_\mathrm{t} := \frac{\partial f_\mathrm{a}}{\partial \boldsymbol{t}_\mathrm{t}} = \frac{\partial f_\mathrm{r}}{\partial \boldsymbol{t}_\mathrm{t}} = \boldsymbol{m}_\mathrm{c} \ . \tag{37}$$

Since $\boldsymbol{n}_\mathrm{t} = \boldsymbol{m}_\mathrm{c}$, (36) only provides the change of $\boldsymbol{\xi}_\mathrm{s}$ along $\boldsymbol{m}_\mathrm{c}$. Since for liquids the contact line can also move along its tangent direction $\bar{\boldsymbol{a}}_\mathrm{c}$, (36) needs to be modified into

$$\dot{\xi}^\alpha_\mathrm{s} = (\lambda\, \boldsymbol{m}_\mathrm{c} + \lambda^a\, \bar{\boldsymbol{a}}_\mathrm{c}) \cdot \boldsymbol{a}^\alpha_\mathrm{s} \ , \tag{38}$$

where λ^a denotes the sliding velocity along $\bar{\boldsymbol{a}}_\mathrm{c}$. During the time step from t_n to t_{n+1} velocity λ^a causes the (frictionless) sliding amount $\Delta\lambda^a_{n+1} := \Delta t_{n+1}\lambda^a$ which is equal to

$$\Delta\lambda^a_{n+1} = \bar{\boldsymbol{a}}^{n+1}_\mathrm{c} \cdot \left(\boldsymbol{x}^{n+1}_\mathrm{p} - \boldsymbol{x}^{n+1}_\mathrm{m}(\boldsymbol{\xi}^n_\mathrm{s})\right). \tag{39}$$

Also here one can simply replace $\boldsymbol{x}_\mathrm{p}$ by $\boldsymbol{x}_\mathrm{c}$. Using implicit Euler to integrate evolution law (38) gives

$$\xi^\alpha_{\mathrm{s}\,n+1} = \xi^\alpha_{\mathrm{s}\,n} + \left(\Delta\lambda_{n+1}\,\boldsymbol{m}^{n+1}_\mathrm{c} + \Delta\lambda^a_{n+1}\,\bar{\boldsymbol{a}}^{n+1}_\mathrm{c}\right) \cdot \boldsymbol{a}^\alpha_{\mathrm{s}\,n+1}\ . \tag{40}$$

This corresponds to the update formula for point $\boldsymbol{x}_\mathrm{m}(\boldsymbol{\xi}_\mathrm{s})$

$$\boldsymbol{x}^{n+1}_\mathrm{m}(\boldsymbol{\xi}^{n+1}_\mathrm{s}) = \boldsymbol{x}^{n+1}_\mathrm{m}(\boldsymbol{\xi}^n_\mathrm{s}) + \Delta\lambda_{n+1}\,\boldsymbol{m}^{n+1}_\mathrm{c} + \Delta\lambda^a_{n+1}\,\bar{\boldsymbol{a}}^{n+1}_\mathrm{c}\ . \tag{41}$$

Inserting this into Eq. (34) gives

$$\boldsymbol{t}^{n+1}_\mathrm{t} = \boldsymbol{t}^\mathrm{trial}_{\mathrm{t}\,n+1} - \epsilon_\mathrm{t}\,\Delta\lambda_{n+1}\,\boldsymbol{m}^{n+1}_\mathrm{c}\ . \tag{42}$$

Enforcing $f^{n+1}_\mathrm{a} = 0$ in case of advancing and $f^{n+1}_\mathrm{r} = 0$ in case of receding, then gives

$$\Delta\lambda_{n+1} = \begin{cases} f^\mathrm{trial}_{\mathrm{a}\,n+1}/\epsilon_\mathrm{t} & \text{advancing,} \\ f^\mathrm{trial}_{\mathrm{r}\,n+1}/\epsilon_\mathrm{t} & \text{receding.} \end{cases} \tag{43}$$

Inserting this into (42) correctly reproduces the sliding friction laws

$$\boldsymbol{t}^{n+1}_\mathrm{t} = \begin{cases} \gamma_\mathrm{a}\,\boldsymbol{m}^{n+1}_\mathrm{c} & \text{advancing,} \\ \gamma_\mathrm{r}\,\boldsymbol{m}^{n+1}_\mathrm{c} & \text{receding,} \end{cases} \tag{44}$$

that are inherent to (26). The computational algorithm that follows from the above expressions is summarized in Tab. 1. For simplification, $\boldsymbol{a}^\alpha_{\mathrm{s}\,n+1}$ can be replaced by $\boldsymbol{a}^\alpha_{\mathrm{p}\,n+1}$ as noted in Sauer and De Lorenzis (2015).

Remark 5: Unlike solids, the frictional contact traction $\boldsymbol{t}_\mathrm{t}$ for liquids is always perpendicular to the contact line $\mathcal{C}$ (i.e. parallel to direction $\boldsymbol{m}_\mathrm{c}$). Thus, it is not necessarily parallel to the sliding direction, as is the case for the classical Coulomb law.

Remark 6: In general, even when only considering mechanical effects, the limit values θ_a and θ_r (or γ_a and γ_r) can be functions of location (surface heterogeneity), sliding direction (surface anisotropy) or sliding velocity. The later case accounts for the difference between static and dynamic friction as can be experimentally observed (Dussan V., 1979).

Remark 7: The algorithm of Tab. 1 can be simplified at a small increase of storage requirements. Instead of tracking $\boldsymbol{\xi}_\mathrm{s}$, one can directly track $\boldsymbol{x}_\mathrm{s} := \boldsymbol{x}_\mathrm{m}(\boldsymbol{\xi}_\mathrm{s})$ according to Eq. (41). If $\partial\mathcal{B}$ is immobile, this simplifies to

$$\boldsymbol{x}^{n+1}_\mathrm{s} = \boldsymbol{x}^n_\mathrm{s} + \Delta\lambda_{n+1}\,\boldsymbol{m}^{n+1}_\mathrm{c} + \bar{\boldsymbol{a}}^{n+1}_\mathrm{c} \otimes \bar{\boldsymbol{a}}^{n+1}_\mathrm{c}\left(\boldsymbol{x}^{n+1}_\mathrm{c} - \boldsymbol{x}^n_\mathrm{s}\right)\ , \tag{45}$$

This simplification is especially useful if one wants to avoid parameterizing $\partial\mathcal{B}$, which is possible for simple surfaces, like planes and cylinder surfaces.

Remark 8: The algorithm of Tab. 1 takes a kinetic viewpoint by characterizing the trial state by the traction $\boldsymbol{t}^\mathrm{trial}_\mathrm{t}$ as is common for friction algorithms used for solids. Alternatively, a purely kinematic viewpoint can be taken by characterizing the trial state by the angle $\theta^\mathrm{trial}_\mathrm{c}$. In this

1. Given starting values

$\boldsymbol{x}_{\mathrm{c}}^{n+1}$, $\bar{\boldsymbol{a}}_{\mathrm{c}}^{n+1}$, $\boldsymbol{n}_{\mathrm{c}}^{n+1}$, $\boldsymbol{m}_{\mathrm{c}}^{n+1}$	current location and orthonormal basis of a point on $\mathcal{C}$
$\boldsymbol{x}_{\mathrm{m}}^{n+1} = \boldsymbol{x}_{\mathrm{m}}^{n+1}(\boldsymbol{\xi})$	current surface description of $\partial\mathcal{B}$
$\boldsymbol{\xi}_{\mathrm{p}}^{n+1} = \left(\xi_{\mathrm{p}}^1, \xi_{\mathrm{p}}^2\right)_{n+1}$	current projection point coordinates for $\boldsymbol{x}_{\mathrm{c}}^{n+1}$ given by (12)
$\boldsymbol{a}_{\mathrm{p}\,n+1}^{\alpha}$	contra-variant tangent vectors of $\partial\mathcal{B}$ at $\boldsymbol{x}_{\mathrm{p}}^{n+1} = \boldsymbol{x}_{\mathrm{m}}^{n+1}(\boldsymbol{\xi}_{\mathrm{p}}^{n+1})$
γ_{a}, γ_{r}	(current) surface tension limits at $\boldsymbol{\xi}_{\mathrm{p}}^{n+1}$ according to (23)
$\boldsymbol{\xi}_{\mathrm{s}}^{n} = \left(\xi_{\mathrm{s}}^1, \xi_{\mathrm{s}}^2\right)_{n}$	coordinates of the sliding point at the previous time step

2. Sliding amount along $\boldsymbol{m}_{\mathrm{c}}$ and $\bar{\boldsymbol{a}}_{\mathrm{c}}$

$$\Delta\lambda_{n+1}^{\mathrm{trial}} = \boldsymbol{m}_{\mathrm{c}}^{n+1} \cdot \left(\boldsymbol{x}_{\mathrm{c}}^{n+1} - \boldsymbol{x}_{\mathrm{m}}^{n+1}(\boldsymbol{\xi}_{\mathrm{s}}^{n})\right); \quad \Delta\lambda_{n+1}^{a} = \bar{\boldsymbol{a}}_{\mathrm{c}}^{n+1} \cdot \left(\boldsymbol{x}_{\mathrm{c}}^{n+1} - \boldsymbol{x}_{\mathrm{m}}^{n+1}(\boldsymbol{\xi}_{\mathrm{s}}^{n})\right)$$

3. Elastic predictor

$$\boldsymbol{t}_{\mathrm{t}\,n+1}^{\mathrm{trial}} = \epsilon_{\mathrm{t}}\,\Delta\lambda_{n+1}^{\mathrm{trial}}\,\boldsymbol{m}_{\mathrm{c}}^{n+1}\,; \quad \theta_{\mathrm{c}\,n+1}^{\mathrm{trial}} = \arccos\left(\cos\theta_{\mathrm{c}}^{0} - \epsilon_{\mathrm{t}}\,\Delta\lambda_{n+1}^{\mathrm{trial}}/\gamma_{\mathrm{LG}}\right)$$

4. Check slip criteria and perform correction

$$f_{\mathrm{a}\,n+1}^{\mathrm{trial}} = \boldsymbol{t}_{\mathrm{t}\,n+1}^{\mathrm{trial}} \cdot \boldsymbol{m}_{\mathrm{c}}^{n+1} - \gamma_{\mathrm{a}} \quad \text{(slip function for advancing)}$$

$$f_{\mathrm{r}\,n+1}^{\mathrm{trial}} = \boldsymbol{t}_{\mathrm{t}\,n+1}^{\mathrm{trial}} \cdot \boldsymbol{m}_{\mathrm{c}}^{n+1} - \gamma_{\mathrm{r}} \quad \text{(slip function for receding)}$$

if $f_{\mathrm{a}\,n+1}^{\mathrm{trial}} \leq 0$ and $f_{\mathrm{r}\,n+1}^{\mathrm{trial}} \geq 0$: sticking state with $\Delta\lambda_{n+1} = 0$ and $\theta_{\mathrm{c}}^{n+1} = \theta_{\mathrm{c}\,n+1}^{\mathrm{trial}}$

if $f_{\mathrm{a}\,n+1}^{\mathrm{trial}} > 0$: advancing state with $\Delta\lambda_{n+1} = f_{\mathrm{a}\,n+1}^{\mathrm{trial}}/\epsilon_{\mathrm{t}}$ and $\theta_{\mathrm{c}}^{n+1} = \theta_{\mathrm{a}}$

if $f_{\mathrm{r}\,n+1}^{\mathrm{trial}} < 0$: receding state with $\Delta\lambda_{n+1} = f_{\mathrm{r}\,n+1}^{\mathrm{trial}}/\epsilon_{\mathrm{t}}$ and $\theta_{\mathrm{c}}^{n+1} = \theta_{\mathrm{r}}$

5. Update tangential slip and tractions

$$\xi_{\mathrm{s}\,n+1}^{\alpha} = \xi_{\mathrm{s}\,n}^{\alpha} + \left(\Delta\lambda_{n+1}\,\boldsymbol{m}_{\mathrm{c}}^{n+1} + \Delta\lambda_{n+1}^{a}\,\bar{\boldsymbol{a}}_{\mathrm{c}}^{n+1}\right) \cdot \boldsymbol{a}_{\mathrm{p}\,n+1}^{\alpha}$$

$$\boldsymbol{t}_{\mathrm{t}}^{n+1} = \boldsymbol{t}_{\mathrm{t}\,n+1}^{\mathrm{trial}} - \epsilon_{\mathrm{t}}\,\Delta\lambda_{n+1}\,\boldsymbol{m}_{\mathrm{c}}^{n+1}\,, \quad \boldsymbol{q}_{\mathrm{c}}^{n+1} = \boldsymbol{q}_{\mathrm{c}}^{0} - \boldsymbol{t}_{\mathrm{t}}^{n+1} + \gamma_{\mathrm{LG}}\left(\sin\theta_{\mathrm{c}}^{0} - \sin\theta_{\mathrm{c}}^{n+1}\right)\boldsymbol{n}_{\mathrm{c}}^{n+1}$$

Table 1: Predictor-corrector (stick-slip) algorithm for the computation of the tangential contact state at the contact line point $\boldsymbol{x}_{\mathrm{c}} \in \mathcal{C}$. Alternative formulations are given in remarks 7, 8 & 9.

case, $\boldsymbol{t}_{\mathrm{t}}^{\mathrm{trial}}$ and $\boldsymbol{t}_{\mathrm{t}}$ are not needed and we can simply replace the expressions for $f_{\mathrm{a}\,n+1}^{\mathrm{trial}}$, $f_{\mathrm{r}\,n+1}^{\mathrm{trial}}$, $\Delta\lambda_{n+1}$ and $\boldsymbol{q}_{\mathrm{c}}^{n+1}$ in Tab. 1 by the equivalent expressions

$$\begin{aligned}
\bar{f}_{\mathrm{a}\,n+1}^{\mathrm{trial}} &= \cos\theta_{\mathrm{a}} - \cos\theta_{\mathrm{c}\,n+1}^{\mathrm{trial}}\,, \\
\bar{f}_{\mathrm{r}\,n+1}^{\mathrm{trial}} &= \cos\theta_{\mathrm{r}} - \cos\theta_{\mathrm{c}\,n+1}^{\mathrm{trial}}\,, \\
\Delta\lambda_{n+1} &= \Delta\lambda_{n+1}^{\mathrm{trial}} - \gamma_{\mathrm{a}}/\epsilon_{\mathrm{t}} \quad \text{for advancing,} \\
\Delta\lambda_{n+1} &= \Delta\lambda_{n+1}^{\mathrm{trial}} - \gamma_{\mathrm{r}}/\epsilon_{\mathrm{t}} \quad \text{for receding,} \\
\boldsymbol{q}_{\mathrm{c}}^{n+1} &= \left(\gamma_{\mathrm{SL}} + \gamma_{\mathrm{LG}}\cos\theta_{\mathrm{c}}^{n+1}\right)\boldsymbol{m}_{\mathrm{c}}^{n+1} - \gamma_{\mathrm{LG}}\sin\theta_{\mathrm{c}}^{n+1}\,\boldsymbol{n}_{\mathrm{c}}^{n+1}\,.
\end{aligned} \tag{46}$$

Remark 9: In case an *open droplet contact model* is considered (according to Fig. 2a), the definition of line load $\boldsymbol{q}_{\mathrm{c}}$ needs to be changed into

$$\boldsymbol{q}_{\mathrm{c}} = \gamma_{\mathrm{LG}}\cos\theta_{\mathrm{c}}\,\boldsymbol{m}_{\mathrm{c}} - \gamma_{\mathrm{LG}}\sin\theta_{\mathrm{c}}\,\boldsymbol{n}_{\mathrm{c}}\,. \tag{47}$$

5 Finite element formulation

The membrane and contact models of Secs. 2 and 4 are discretized and solved with the finite element method following the formulation of Sauer et al. (2014) and Sauer (2014). This section summarises the resulting FE equations accounting for the friction algorithm of Tab. 1. The substrate surface is considered to be rigid and immobile, so that it does not need to be discretized and linearized.

The membrane surface $\mathcal{S}$ is discretized into n_{se} surface elements, denoted as Ω^e in the current configuration and Ω_0^e in the reference configuration (with $e = 1, ..., n_{\text{se}}$). Within those, the geometry is approximated by

$$\begin{aligned} \boldsymbol{X} &\approx \mathbf{N}\,\mathbf{X}_e\ , \quad & \boldsymbol{X} &\in \Omega_0^e\ , \\ \boldsymbol{x} &\approx \mathbf{N}\,\mathbf{x}_e\ , \quad & \boldsymbol{x} &\in \Omega^e\ , \end{aligned} \tag{48}$$

where $\mathbf{N} := [N_1\mathbf{1},\, N_2\mathbf{1},\, ...,\, N_{n_e}\mathbf{1}]$ contains the n_e shape functions $N_I = N_I(\xi^1, \xi^2)$, and $\mathbf{X}_e$ and $\mathbf{x}_e$ contain the n_e initial and current nodal positions of the surface element. Consequently

$$\begin{aligned} \boldsymbol{A}_\alpha &\approx \mathbf{N}_{,\alpha}\,\mathbf{X}_e\ , \\ \boldsymbol{a}_\alpha &\approx \mathbf{N}_{,\alpha}\,\mathbf{x}_e\ , \end{aligned} \tag{49}$$

where $\mathbf{N}_{,\alpha} = [N_{1,\alpha}\mathbf{1},\, N_{2,\alpha}\mathbf{1},\, ...,\, N_{n_e,\alpha}\mathbf{1}]$. The variation $\boldsymbol{w}$ is approximated analogously, i.e.

$$\begin{aligned} \boldsymbol{w} &\approx \mathbf{N}\,\mathbf{w}_e\ , \\ \boldsymbol{w}_{;\alpha} = \boldsymbol{w}_{,\alpha} &\approx \mathbf{N}_{,\alpha}\,\mathbf{w}_e\ . \end{aligned} \tag{50}$$

This leads to

$$w_{\alpha;\beta} \approx \mathbf{w}_e^{\mathrm{T}}\,\mathbf{N}_{,\beta}^{\mathrm{T}}\,\boldsymbol{a}_\alpha + b_{\alpha\beta}\,\mathbf{w}_e^{\mathrm{T}}\,\mathbf{N}^{\mathrm{T}}\,\boldsymbol{n}\ , \tag{51}$$

where $b_{\alpha\beta} = \boldsymbol{n}\cdot\boldsymbol{a}_{\alpha,\beta}$ characterizes the curvature of surface $\mathcal{S}$.
Likewise, boundary $\partial_t\mathcal{B}$ and contact line $\mathcal{C}$ are discretized into n_{te} and n_{ce} line elements, denoted as Γ_t^e (with $e - n_{\text{se}} = 1, ..., n_{\text{te}}$) and Γ_{c}^e (with $e - n_{\text{se}} - n_{\text{te}} = 1, ..., n_{\text{ce}}$) in the current configuration. Within those

$$\begin{aligned} \boldsymbol{x}_{\text{c}} &\approx \mathbf{N}_{\text{t}}\,\mathbf{x}_e\ , \\ \boldsymbol{a}_{\text{c}} &\approx \mathbf{N}_{\text{t},\xi}\,\mathbf{x}_e\ , \\ \boldsymbol{w} &\approx \mathbf{N}_{\text{t}}\,\mathbf{w}_e\ , \end{aligned} \tag{52}$$

where $\mathbf{N}_{\text{t}} := [N_1\mathbf{1},\, N_2\mathbf{1},\, ...,\, N_{n_e}\mathbf{1}]$ and $\mathbf{N}_{\text{t},\xi} = [N_{1,\xi}\mathbf{1},\, N_{2,\xi}\mathbf{1},\, ...,\, N_{n_e,\xi}\mathbf{1}]$ contain the n_e shape functions $N_I = N_I(\xi)$ and their derivatives, and $\mathbf{x}_e$ and $\mathbf{w}_e$ contain the n_e nodal positions and variations of the line element.

The weak form of Eqs. (5) and (6) is thus discretized as

$$G \approx \sum_{e=1}^{n_{\text{se}}+n_{\text{te}}+n_{\text{ce}}} G^e\ , \tag{53}$$

where

$$G^e = \mathbf{w}_e^{\mathrm{T}}\left[\mathbf{f}_{\text{int}}^e + \mathbf{f}_{\text{sta}}^e + \mathbf{f}_{\text{c}}^e - \mathbf{f}_{\text{f}}^e - \mathbf{f}_{\text{ext}}^e\right]\ , \tag{54}$$

is the contribution from surface element Ω^e and line elements Γ_t^e and Γ_{c}^e. It is composed of the

FE force vectors

$$
\begin{aligned}
\mathbf{f}^e_{\text{int}} &= \int_{\Omega^e} \gamma\, \mathbf{N}^{\mathrm{T}}_{,\alpha}\, \boldsymbol{a}^\alpha \,\mathrm{d}a \;, \\
\mathbf{f}^e_{\text{sta}} &= \int_{\Omega^e} \sigma^{\alpha\beta}_{\text{sta}} \left(\mathbf{N}^{\mathrm{T}}_{,\alpha}\, \boldsymbol{a}_\beta + b_{\alpha\beta}\, \mathbf{N}^{\mathrm{T}} \boldsymbol{n} \right) \mathrm{d}a \;, \\
\mathbf{f}^e_{\text{c}} &= -\int_{\Omega^e} \mathbf{N}^{\mathrm{T}}\, f^\alpha_{\text{c}}\, \boldsymbol{a}_\alpha \,\mathrm{d}a + \int_{\Omega^e} \mathbf{N}^{\mathrm{T}}\, p_{\text{c}}\, \boldsymbol{n} \,\mathrm{d}a \;, \\
\mathbf{f}^e_{\text{f}} &= \int_{\Omega^e} \mathbf{N}^{\mathrm{T}}\, f^\alpha_{\text{f}}\, \boldsymbol{a}_\alpha \,\mathrm{d}a + \int_{\Omega^e} \mathbf{N}^{\mathrm{T}}\, p_{\text{f}}\, \boldsymbol{n} \,\mathrm{d}a \;, \\
\mathbf{f}^e_{\text{ext}} &= \int_{\Omega^e} \mathbf{N}^{\mathrm{T}}\, \bar{f}^\alpha\, \boldsymbol{a}_\alpha \,\mathrm{d}a - \int_{\Omega^e} \mathbf{N}^{\mathrm{T}}\, \bar{p}\, \boldsymbol{n} \,\mathrm{d}a + \int_{\Gamma^e_{\bar{t}}} \mathbf{N}^{\mathrm{T}}_{\text{t}}\, \bar{\boldsymbol{t}} \,\mathrm{d}s + \int_{\Gamma^e_{\text{c}}} \mathbf{N}^{\mathrm{T}}_{\text{t}}\, \boldsymbol{q}_{\text{c}} \,\mathrm{d}s \;.
\end{aligned}
\tag{55}
$$

For the quasi-static case $f^\alpha_c = f^\alpha_f = 0$. Further, if no external loads are considered apart from line load $\boldsymbol{q}_{\text{c}}$, then $\bar{f}^\alpha = \bar{p} = 0$ and $\bar{\boldsymbol{t}} = \mathbf{0}$. This is the case for the examples in Secs. 6.1 and 6.2. For the examples in Secs. 6.3 and 6.4 the external pressure $\bar{p}$ is given by (58). The fluid pressure is given by (9), while the contact pressure follows from (14). The contact line load $\boldsymbol{q}_{\text{c}}$ is computed from the friction algorithm of Tab. 1.

The FE force vectors are assembled into global force vectors. The resulting equation at the free nodes (where no Dirichlet BC are applied) then becomes

$$
\mathbf{f}(\boldsymbol{x}, p_{\text{v}}) = \mathbf{f}_{\text{int}}(\mathbf{x}) + \mathbf{f}_{\text{sta}}(\mathbf{x}) + \mathbf{f}_{\text{c}}(\mathbf{x}) - \mathbf{f}_{\text{f}}(\mathbf{x}, p_{\text{v}}) - \mathbf{f}_{\text{ext}}(\mathbf{x}) = \mathbf{0} \;, \tag{56}
$$

which is solved together with volume constraint (10) for the unknown nodal positions $\mathbf{x}$ and the single pressure unknown p_{v}. For closed droplets, the volume can be computed from (Sauer et al., 2014)

$$
V \approx \frac{1}{3} \sum_{e=1}^{n_{\text{se}}} \int_{\Omega^e} \boldsymbol{x} \cdot \boldsymbol{n} \,\mathrm{d}a \;. \tag{57}
$$

For open droplets, this formula only accounts for the volume of the cone extending from the origin to $\mathcal{S}$. The Newton-Raphson method is used for solving (56) and (10) monolithically. Therefore the entire system needs to be linearized with respect to $\mathbf{x}$ and p_{v}. The linearization of $\mathbf{f}^e_{\text{int}}$, $\mathbf{f}^e_{\text{sta}}$, $\mathbf{f}^e_{\text{c}}$ and $\mathbf{f}^e_{\text{ext}}$ is given in Appendix A. The linearization of $\mathbf{f}_{\text{f}}$ and g_{v} can be taken directly from Sauer (2014).

6 Numerical examples

This section presents several numerical examples in order to demonstrate the performance of the friction algorithm of Tab. 1. The examples are marked by increasing complexity.

6.1 Droplet inflation

The first example considers the inflation of a droplet in contact with a flat, homogeneous substrate surface. Under these contact conditions, the droplet remains axisymmetric during inflation, such that the contact state (and angle) is uniform along $\mathcal{C}$. No gravity loading is considered, such that the droplet remains spherical and an analytical solution is available for reference. The problem is a simple and natural first test case for the proposed sliding algorithm. A similar setup is considered in Santos and White (2011); Tadmor (2011); Prabhala et al.

(2013). The initial starting configuration is a hemispherical droplet with contact angle $\theta_c^0 = 90°$, droplet radius L_0, contact radius $a_0 = L_0$, droplet volume $V_0 = 2\pi L_0^3/3$ and internal pressure $p_0 = 2\gamma/L_0$. The advancing and receding contact angles are chosen as $\theta_a = 120°$ and $\theta_r = 60°$. $6m^2$ quadratic Lagrange finite elements are used to model a quarter droplet, considering $m = 2, 4, 8, 16$. The initial configuration for $m = 2$ is shown in Fig. 8A. The penalty parameters for normal surface and tangential line contact are taken as $\epsilon_n = 62.5m^2$ and $\epsilon_t = 25m^2$. Stabilization scheme (8) is used with $\mu = \gamma$.

The simulation starts by increasing the prescribed volume from $V = V_0$ to $V = 5V_0$ considering $n_t = 10m^2$ steps. Thereby the contact radius increases to $a \approx 1.25a_0$. The volume is then decreased until $a = a_0$ again; this happens at $V \approx 0.5V_0$. Then the volume is increased again up to V_0 such that we arrive at the initial starting point. During this loading cycle, the contact line cycles through the states of advancing, pinning and receding. Fig. 8 shows the deformation sequence during this cycle. The figure shows that the droplet shape (but not necessarily the FE

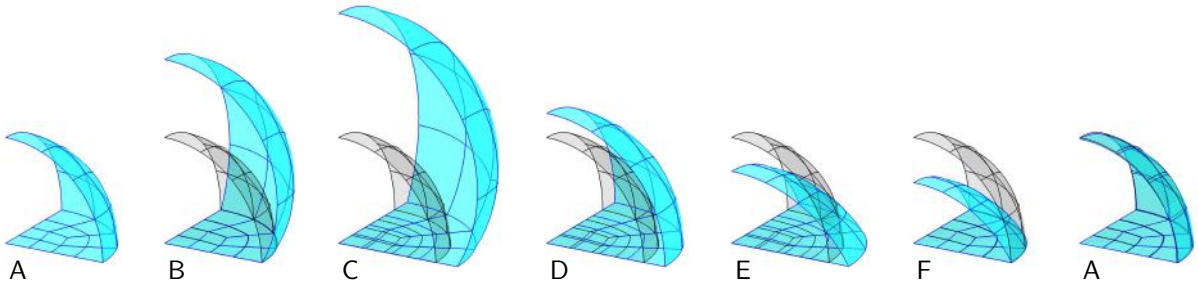

Figure 8: Inflated droplet: deformation cycle A-B-C-D-E-F-A. The initial configuration is shown in grey.

mesh) returns to the initial configuration after a full cycle. Fig. 9 shows the theoretical change of contact radius a and contact angle θ_c in dependency of the prescribed volume V. These

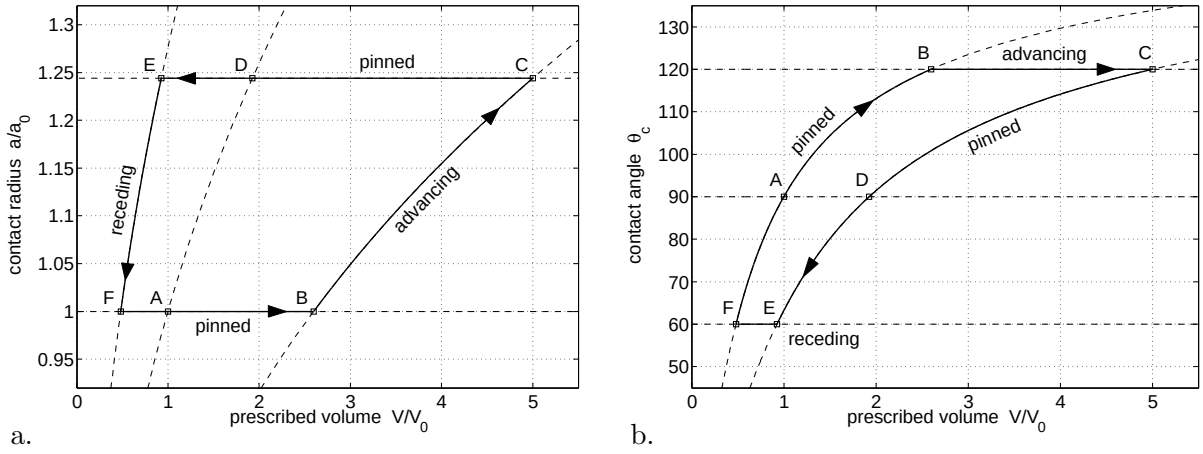

Figure 9: Inflated droplet: (a) contact radius vs. prescribed droplet volume and (b) contact angle vs. prescribed droplet volume along the deformation cycle A-B-C-D-E-F-A (auxilliary lines shown dashed).

relations can be easily obtained analytically, since the free surface of the droplet always remains spherical. Likewise, the pressure-volume relation can be determined analytically. This is shown in Fig 10, comparing the theoretical results to the numerical ones. With a coarse mesh ($m = 2$), a considerable difference occurs between the two. This difference can be assessed by examining

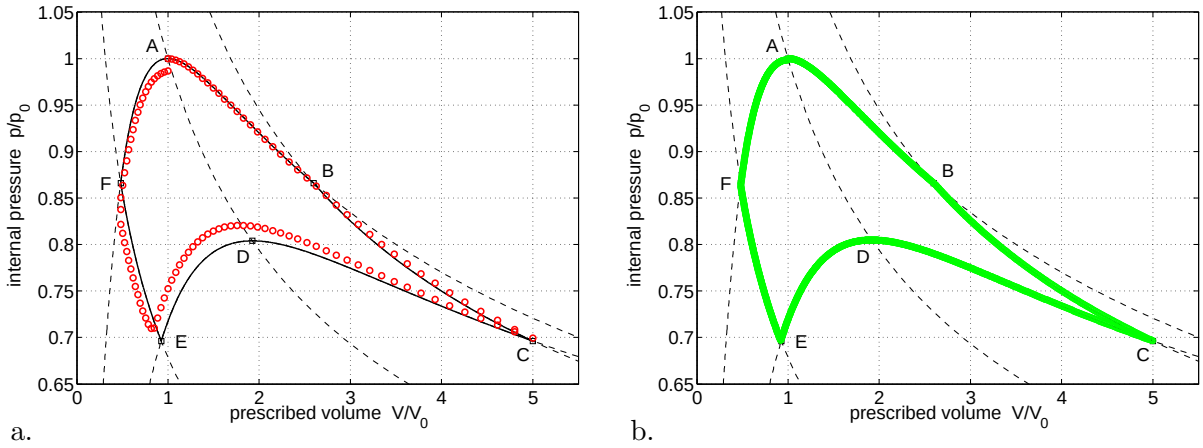

Figure 10: Inflated droplet: internal pressure vs. prescribed droplet volume; comparison between analytical solution (solid line) and FE solution ('$\circ$') considering (a) $m = 2$ and (b) $m = 8$.

the energy dissipated in the cycle A-B-C-D-E-F-A. This energy is given by the area enclosed by the $p(V)$ curve. Fig. 11 shows the error in the dissipation of the numerical result. As expected

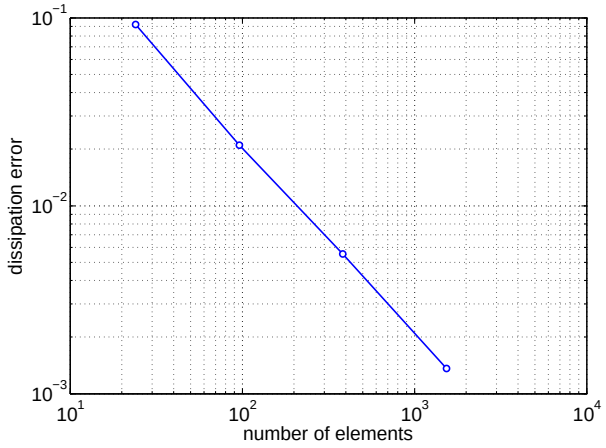

Figure 11: Inflated droplet: convergence of the FE solution to the analytical value of the dissipated energy in cycle A-B-C-D-E-F-A.

it converges with mesh refinement. (Here the load step n_t is decreased along with the element size). The example demonstrates that the proposed algorithm can correctly capture the contact state changes occurring at points B, C, E and F.

6.2 Pinned droplet on an inclined plane

The second example considers an extension of the previous case, where the deformation is now non-axisymmetric and results in a varying contact angle and thus a varying contact state along $\mathcal{C}$. Considered is a gravity-affected droplet on an inclined plane. The inclination β is increased from $\beta = 0$ to $\beta = 360°$. Due to gravity[5] the droplet tilts and possibly begins to slide downward. At

[5]In the simulation, the plane is considered to remain parallel to the $(\boldsymbol{e}_1, \boldsymbol{e}_2)$-plane, while the gravity vector in Eq. (9) rotates according to $\boldsymbol{g} = -g(\sin\beta\,\boldsymbol{e}_1 + \cos\beta\,\boldsymbol{e}_3)$.

each step, quasi-static conditions are assumed such that the fluid pressure is always hydrostatic. Depending on the limits θ_a and θ_r, the sliding either starts at the lower edge or at the upper edge and then progresses along $\mathcal{C}$. It thus tests the capability of the algorithm to handle varying contact conditions along $\mathcal{C}$. There is no analytical solution available for this example.

The droplet is considered to have the fixed volume $V = 2\pi L_0^3/3$ and initial contact angle $\theta_c = 90°$. Without gravity, the contact radius and the droplet height thus are $r = h = L_0$. The gravity loading is considered such that $\rho g L_0^3 = \gamma L_0$. The length scale L_0 and the energy density ρg are used for normalization and don't need to be specified. For water at room temperature, where $\rho g = 9.81\,\mathrm{kN/m^3}$ and $\gamma = 72.8\,\mathrm{mN/m}$, this corresponds to a droplet with $L_0 = 2.72\,\mathrm{mm}$ and $V = 42.3\,\mu\mathrm{l}$. From an initial FE analysis we find that the contact radius and height of the droplet under gravity (for $\theta_c = 90°$) change to $r \approx 1.07\,L_0$ and $h \approx 0.88\,L_0$. Quadratic Lagrange elements are used for the analysis. Due to symmetry only half of the droplet is modeled, using $12m^2$ finite elements, where $m = 4$, 8 and 16 have been used. The load step size was taken as $n_t = 1/m$ per degree. Surface contact is modeled with 3×3 quadrature points per Ω^e and $\epsilon_n = 250m^2\rho g$. Line contact is modeled with 3 quadrature points per Γ^e and $\epsilon_t = 25m\,\rho g L_0$. Stabilization scheme 'P' (Sauer, 2014) with a mesh update based on (8) at every load step is used. In the following plots, the deformation is shown for $m = 4$, while θ_c is shown for $m = 8$.

6.2.1 Full pinning

Fig. 12 shows the droplet deformation for the case that the contact line remains fully pinned. The evolution of the deformation can also be seen in the supplementary movie file `drop1.mpg`.

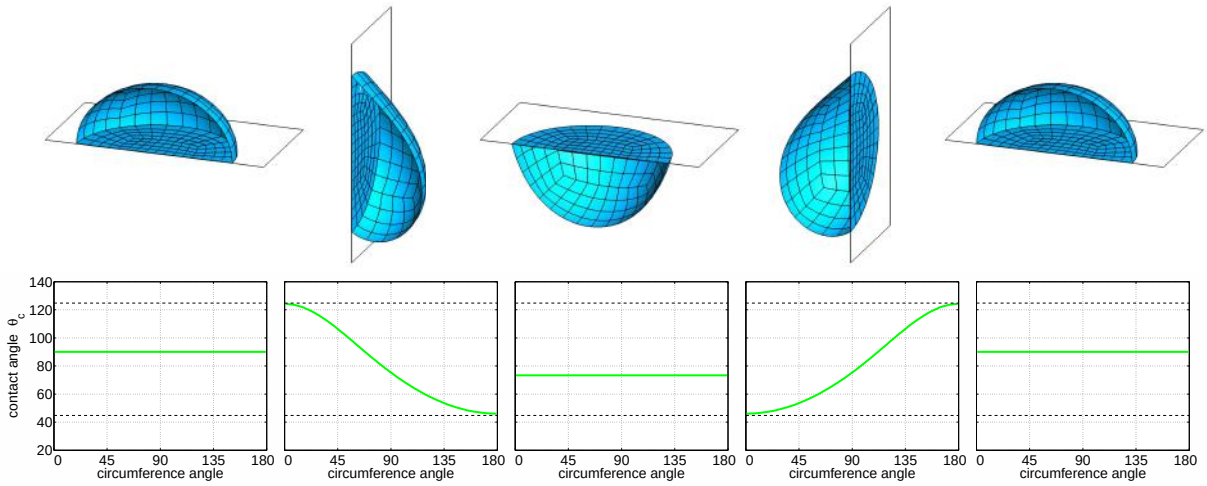

Figure 12: Inclined droplet, fully pinned: droplet configuration (top) and contact angle $\theta_c(\Phi)$ (bottom) at inclinations $\beta = 0°$, 90°, 180°, 270°, 360°. The dashed lines indicate the two extrema, 44.7° and 124.8°, attained by θ_c as β varies (see also Fig. 13).

For the considered parameters the droplet remains fully pinned if $\theta_a \geq 124.8°$ and $\theta_r \leq 44.7°$. These limits can be found by examining the contact angle at the front and rear edges of the droplet as it changes with β. This is shown in Fig. 13. The figure also contains the two cases discussed in the following section. It is also interesting to look at the contact angle as it changes along the contact line. This is shown in the bottom row of Fig. 12. After a full cycle ($\beta = 360°$) the contact angle returns uniformly to its initial value of 90°.

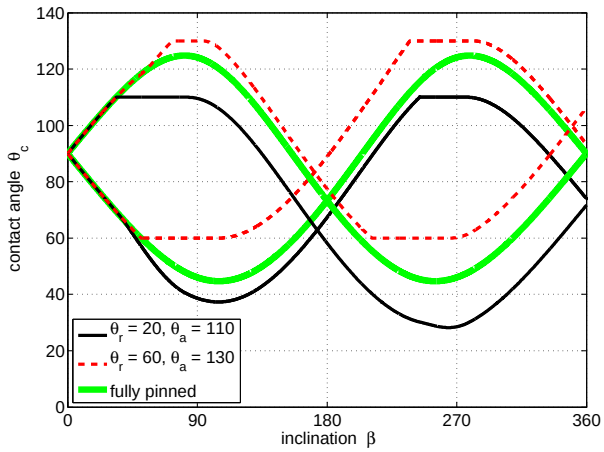

Figure 13: Inclined droplet: contact angle at the front ($\Phi = 0$) and rear ($\Phi = 180°$) of the droplet in dependence of inclination β for the three cases shown in Figs. 12, 14 and 15.

6.2.2 Partial pinning and sliding

If θ_a or θ_r are beyond the limit values identified above, the contact line start to slide. This is considered next. Apart from θ_r and θ_a, the parameters from above are taken. Fig. 14 shows the deformation and contact angle for the case $\theta_r = 20°$ and $\theta_a = 110°$. For these parameters, the

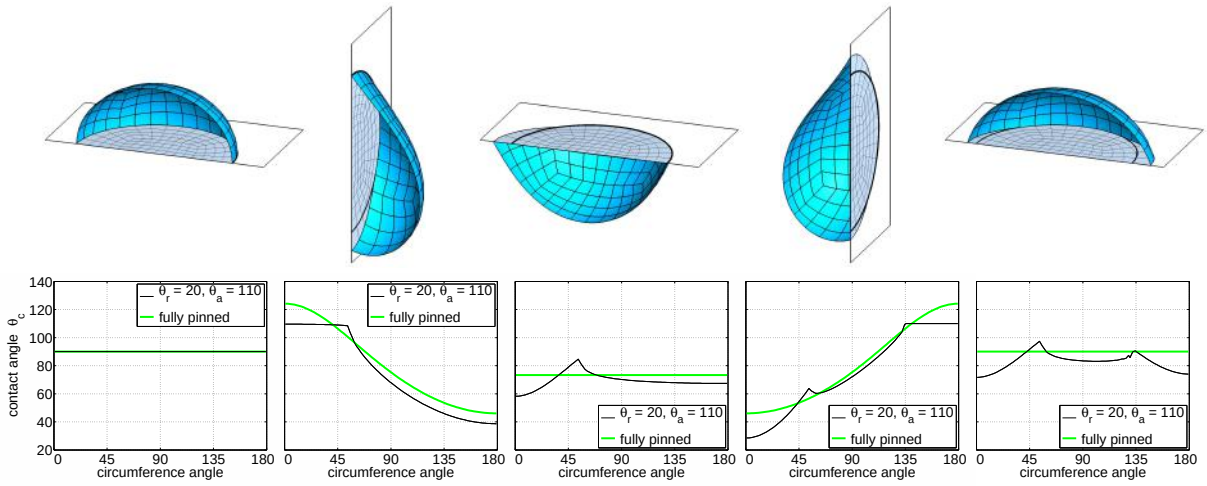

Figure 14: Inclined droplet, partially sliding ($\theta_r = 20°$, $\theta_a = 110°$): droplet configuration (top) and contact angle $\theta_c(\Phi)$ (bottom) at inclinations $\beta = 0°$, 90°, 180°, 270°, 360°. For reference, the results of the pinned case are marked by bold lines (black in top row, green in bottom row).

droplet starts advancing at the lower edge. This happens at an inclination of $\beta \approx 33.7°$. The advancement stops again at 83.0°, then starts at the opposite edge at 244.3° and stops there at 277.6° (see Fig. 13). The evolution of the deformation can also be seen in the supplementary movie file `drop2.mpg`.

Another case, considering $\theta_r = 60°$ and $\theta_a = 120°$ is shown in Fig. 15. Now the upper edge starts receding at $\beta \approx 51.1°$ followed by the advancement of the lower edge at $\beta \approx 72.8°$ (see Fig. 13). The sliding of the two edges stops again at 93.4° and 106.0°, restarts at 211.1° and 237.4° and then stops at 265.2° and 282.0°. The evolution of the deformation for this case can

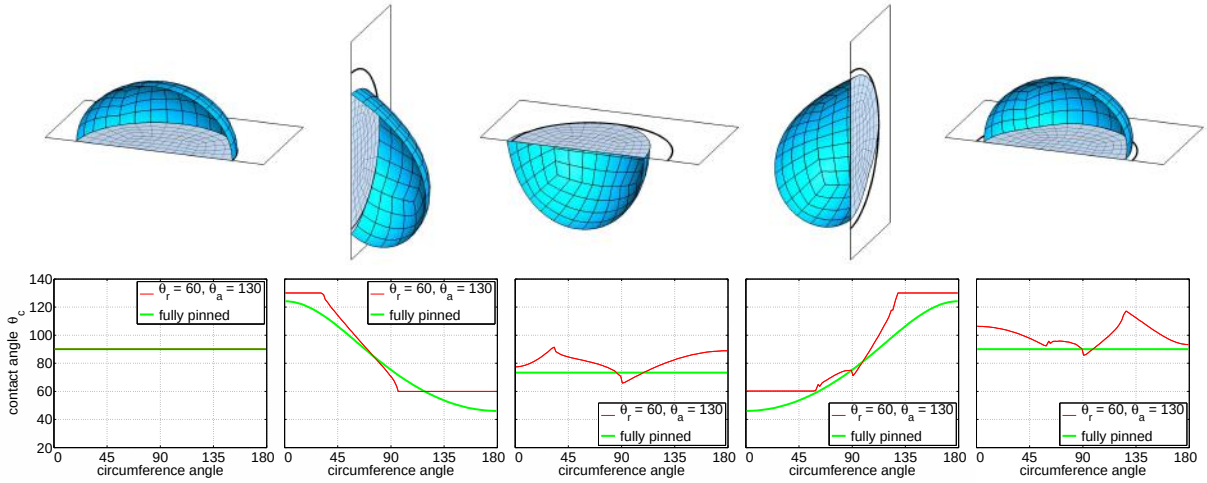

Figure 15: Inclined droplet, partially sliding ($\theta_\mathrm{r} = 60°$, $\theta_\mathrm{a} = 130°$): droplet configuration (top) and contact angle $\theta_\mathrm{c}(\Phi)$ (bottom) at inclinations $\beta = 0°$, $90°$, $180°$, $270°$, $360°$. For reference, the results of the pinned case are marked by bold lines (black in top row, green in bottom row).

also be seen in the supplementary movie file `drop3.mpg`.

The contact angle θ_c at $\Phi = 0$ and $\Phi = 180°$ for the two cases is shown in Fig. 13. It is noted that the $\theta_\mathrm{c}(\Phi)$ curves are in qualitative agreement with the computational results of Janardan and Panchagnula (2014).

6.3 Sliding droplet on an inclined plane

For some values of θ_r, θ_a and β, the entire droplet starts sliding down the inclined plane. This is considered now. It is a further test case for the proposed algorithm. The sliding motion on the inclined plane is inherently dynamic, and cannot be modeled in a quasi-static fashion. Instead it is a dynamic process that requires resisting forces. In general, those can come from the fluid flow within the droplet, from the air flow around the droplet and from frictional sliding forces on the contact surface (see Sec. 3.2). Since the flow field is not modeled explicitly, those forces cannot be computed accurately. But for the purpose of demonstration, one can use the following ad-hoc model to provide resisting forces. Viscous damping is considered by applying the velocity proportional surface pressure

$$\bar{p} = -c\,\boldsymbol{v}\cdot\boldsymbol{n}\ , \tag{58}$$

where c is a damping constant with units of force time per volume. This pressure is simply plugged into FE expression (55.5). In order to discretize the velocity, the first-order rate approximation

$$\boldsymbol{v} \approx \frac{\boldsymbol{x} - \boldsymbol{x}^\mathrm{pre}}{\Delta t} \tag{59}$$

is used, where $\boldsymbol{x}^\mathrm{pre}$ denotes the surface position at the previous time step. Thus

$$\bar{p} \approx -\frac{c}{\Delta t}\boldsymbol{n}\cdot\mathbf{N}\left(\mathbf{x}_e - \mathbf{x}_e^\mathrm{pre}\right)\ . \tag{60}$$

The linearization of this expression – needed for the implicit solution procedure considered here – is given in Appendix A.5.

In the following example the setup and the physical parameters are chosen as in the previous example, taking now $\theta_r = 60°$ and $\theta_a = 110°$. Further, $c = 40\,\rho g T_0$ is considered and the time step $\Delta t = 2T_0/m$ is used, running the simulation until $T = 2000T_0$. Here T_0 is some arbitrary reference time that cancels in the above expressions. To induce sliding, the plane is gradually tilted according to

$$\beta(t) = \begin{cases} t\,\dfrac{\deg}{T_0} & \text{for } t < \beta_0 \dfrac{T_0}{\deg}, \\ \beta_0 & \text{else}, \end{cases} \tag{61}$$

with $\beta_0 = 60°$. Surface contact is now modeled with 3×3 quadrature points per Ω^e and $\epsilon_n = 250m^2\rho g$, while line contact is modeled with 2 quadrature points per Γ^e and $\epsilon_t = 25m\,\rho g L_0$. Stabilization scheme (7) is used with $\mu = 0.05\gamma$. Fig. 16 shows the droplet deformation at various time steps. The evolution of the deformation can also be seen in the supplemental movie file

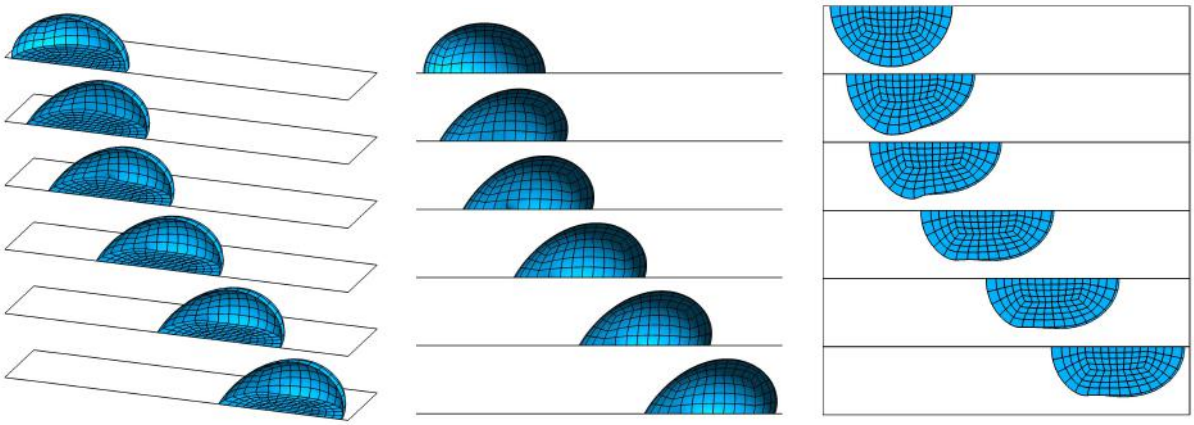

Figure 16: Sliding droplet: 3D view, side view and bottom view (left to right) at $t = \{0, 2, 4, 6, 8, 10\} \cdot 100T_0$ for mesh $m = 4$.

`drop4.mpg`. It takes until $t \approx 1000T_0$ to reach a steady sliding state. In that state the droplet moves with a speed of about $5.75 \cdot 10^{-3} L_0/T_0$. For the parameters given above and, for example, $T_0 = 1\,\text{ms}$, this corresponds to a speed of 15.7 mm/s. Before the steady-state is reached there are considerable changes in the contact angle. This is shown in Fig. 17, which examines $\theta_c(t)$ at selected locations and $\theta_c(\Phi)$ at selected times.

The figure shows that at the advancing ($\Phi = 0$) and receding edges ($\Phi = 180°$) the limit values 110° and 60° are quickly reached, while in the region around $\Phi = 90°$ the transition to steady angles takes much longer. At steady sliding, a very sharp transition between the limit values occurs, which is localized to an interval that is less than 40°. As seen in Fig. 17, oscillations in θ_c occur in both t and Φ. Those are due to the FE discretization, and they decrease upon mesh refinement, which demonstrates the convergence of the proposed contact algorithm. It is noted that the $\theta_c(\Phi)$ curves are in qualitative agreement with the computational results of Dimitrakopoulos and Higdon (1999); Santos and White (2011) and in particular Semprebon and Brinkmann (2014). Also the droplet shape during sliding is in qualitative agreement with the results reported in those works. Qualitative agreement is also found in comparison to the experimental images of Rotenberg et al. (1984) and Extrand and Kumagai (1995). It is noted that during sliding, under certain conditions, small droplet shedding or 'pearling' can occur (Schwartz et al., 2005), which cannot be captured by the current model.

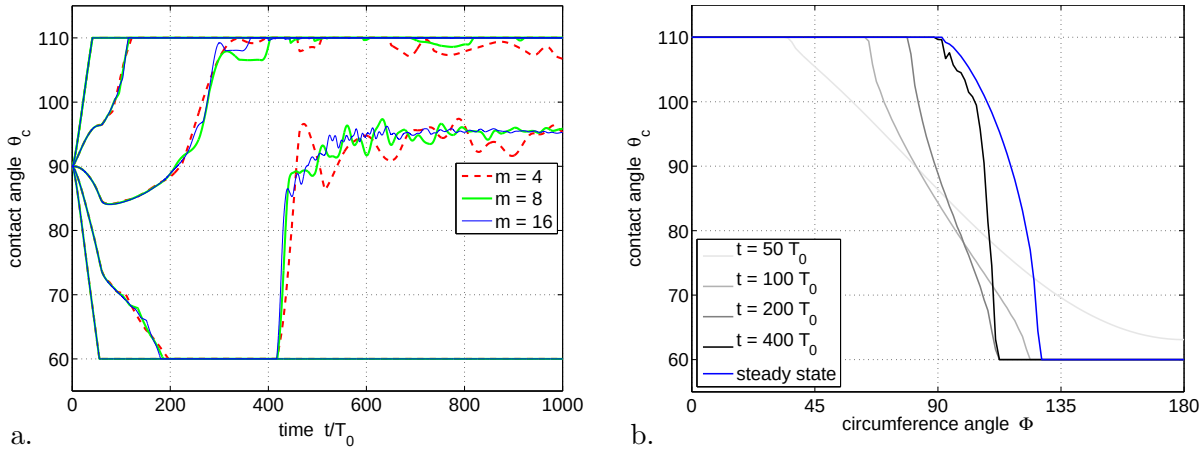

Figure 17: Sliding droplet: Evolution of the contact angle: (a) $\theta_c(t)$ at $\Phi = 0°$, $67.5°$, $90°$, $112.5°$, $180°$ (top to bottom) for various meshes; (b) $\theta_c(\Phi)$ at various t, considering mesh $m = 16$.

6.4 Droplet sliding over a step

So far all the examples have considered flat substrate surfaces. The following example now tests the formulation for curved substrate surfaces. Apart from that, the same setup as in Sec. 6.3, with the physical parameters $\theta_r = 60°$, $\theta_a = 110°$, $V = 2\pi L_0^3/3$, $\rho g L_0^2 = \gamma$, $c = 40\,\rho g T_0$ and $\beta_0 = 75°$, and the numerical parameters $\epsilon_n = 250 m^2 \rho g$, $\epsilon_t = 25 m\,\rho g L_0$ and $\Delta t = T_0/(2m)$, is considered. Again, stabilization scheme (7) is used with $\mu = 0.05\gamma$. On the substrate surface a step is modeled as shown in Fig. 18a. The surface remains straight along y. This surface consists

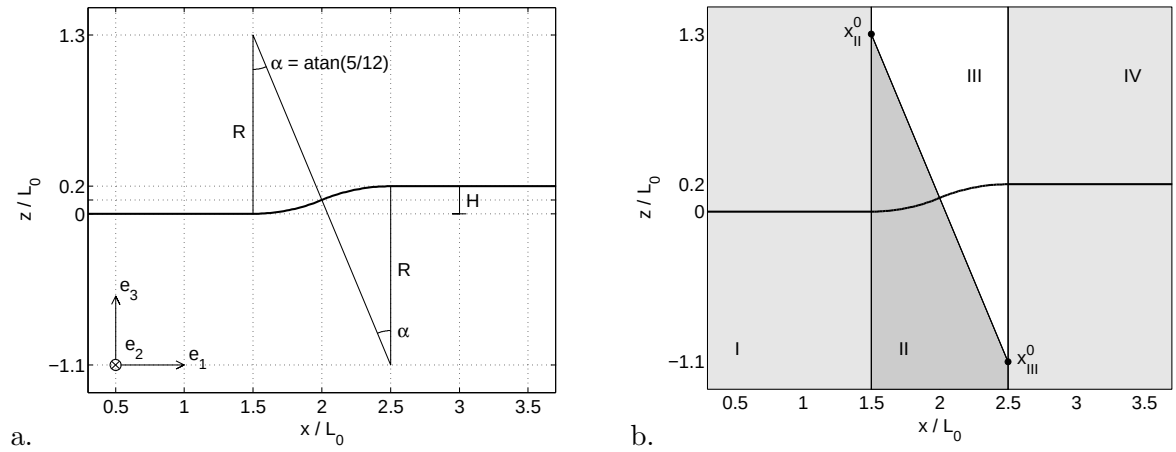

Figure 18: Droplet sliding over a step: (a) step geometry; (b) contact zones.

of cylinder segments, so that the simple update formula (45) can be used. In the four zones shown in Fig. 18b, the contact kinematics is charactized by the quantities given in Tab. 2. Here the $\boldsymbol{e}_2$-component of $\boldsymbol{x}_{\mathrm{II}}$ and $\boldsymbol{x}_{\mathrm{III}}$ is equal to the $\boldsymbol{e}_2$-component of $\boldsymbol{x}_s$, i.e. $\boldsymbol{x}_{\mathrm{II}} = \boldsymbol{x}^0_{\mathrm{II}} + (\boldsymbol{e}_2 \otimes \boldsymbol{e}_2)\boldsymbol{x}_c$ and $\boldsymbol{x}_{\mathrm{III}} = \boldsymbol{x}^0_{\mathrm{III}} + (\boldsymbol{e}_2 \otimes \boldsymbol{e}_2)\boldsymbol{x}_c$. Hence $\boldsymbol{I}_2 := \boldsymbol{e}_1 \otimes \boldsymbol{e}_1 + \boldsymbol{e}_3 \otimes \boldsymbol{e}_3$ is the identity tensor in the $(\boldsymbol{e}_1, \boldsymbol{e}_3)$ plane. Fig. 19 shows the droplet motion and deformation at various time steps. The evolution of the deformation can also be seen in the movie file `drop5.mpg`. There it can be seen that when the advancing edge reaches the step, the drop accelerates, but then slows down considerably since its bulk needs to climb up the step. Once most of the droplet has passed the obstacle, it accelerates again. Since β is larger than in the previous example, the steady state sliding

zone	normal gap	contact normal	gradient of $\boldsymbol{n}_\mathrm{c}$
I	$g_\mathrm{n} = z$	$\boldsymbol{n}_\mathrm{c} = \boldsymbol{e}_3$	$\dfrac{\partial \boldsymbol{n}_\mathrm{c}}{\partial \boldsymbol{x}_\mathrm{c}} = \boldsymbol{0}$
II	$g_\mathrm{n} = R - \Vert\boldsymbol{x}_\mathrm{II} - \boldsymbol{x}_\mathrm{c}\Vert$	$\boldsymbol{n}_\mathrm{c} = \dfrac{\boldsymbol{x}_\mathrm{II} - \boldsymbol{x}_\mathrm{c}}{\Vert\boldsymbol{x}_\mathrm{II} - \boldsymbol{x}_\mathrm{c}\Vert}$	$\dfrac{\partial \boldsymbol{n}_\mathrm{c}}{\partial \boldsymbol{x}_\mathrm{c}} = \dfrac{\boldsymbol{n}_\mathrm{c} \otimes \boldsymbol{n}_\mathrm{c} - \boldsymbol{I}_2}{\Vert\boldsymbol{x}_\mathrm{II} - \boldsymbol{x}_\mathrm{c}\Vert}$
III	$g_\mathrm{n} = \Vert\boldsymbol{x}_\mathrm{c} - \boldsymbol{x}_\mathrm{III}\Vert - R$	$\boldsymbol{n}_\mathrm{c} = \dfrac{\boldsymbol{x}_\mathrm{c} - \boldsymbol{x}_\mathrm{III}}{\Vert\boldsymbol{x}_\mathrm{c} - \boldsymbol{x}_\mathrm{III}\Vert}$	$\dfrac{\partial \boldsymbol{n}_\mathrm{c}}{\partial \boldsymbol{x}_\mathrm{c}} = \dfrac{\boldsymbol{I}_2 - \boldsymbol{n}_\mathrm{c} \otimes \boldsymbol{n}_\mathrm{c}}{\Vert\boldsymbol{x}_\mathrm{c} - \boldsymbol{x}_\mathrm{III}\Vert}$
IV	$g_\mathrm{n} = z - H$	$\boldsymbol{n}_\mathrm{c} = \boldsymbol{e}_3$	$\dfrac{\partial \boldsymbol{n}_\mathrm{c}}{\partial \boldsymbol{x}_\mathrm{c}} = \boldsymbol{0}$

Table 2: Kinematical contact quantities for $\boldsymbol{x}_\mathrm{c} \in \mathcal{C}$ in the different zones.

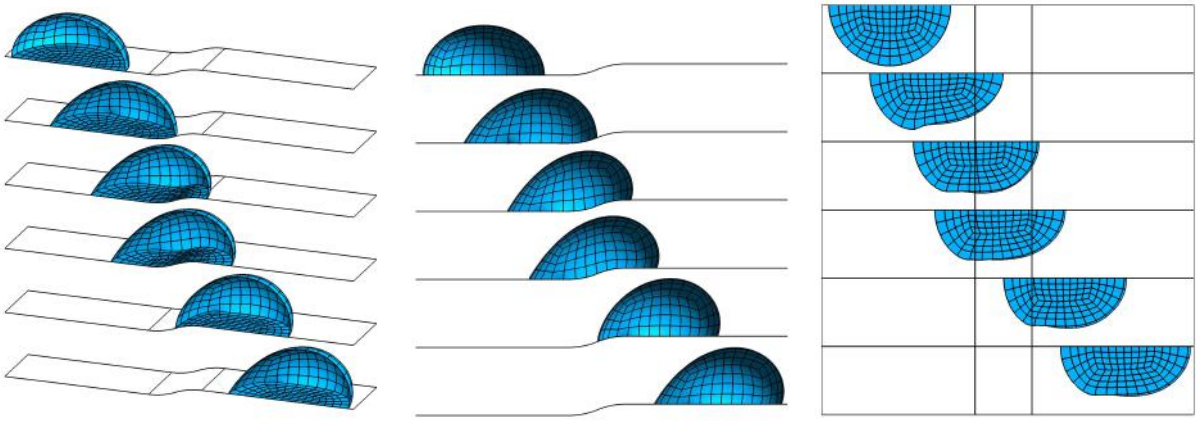

Figure 19: Droplet sliding over a step: different views of the deformation at $t = \{0, 196, 320, 466, 632, 750\}\, T_0$ for mesh $m = 4$.

velocity is larger than before. If $\beta_0 = 60°$, as in the example before, the droplet gets trapped at the step. Tested were also the cases $\beta_0 = 65°$ (droplet is trapped at the step) and $\beta_0 = 70°$ (droplet moves over the step).
The example confirms that the algorithm of Tab. 1 can also handle curved substrate surfaces.

7 Conclusion

This work presents a new and general friction algorithm for liquid-solid contact. It is based on a classical predictor-corrector scheme to enforce the contact conditions at the interface. Under hydrostatic conditions, frictional forces occur only along the contact line $\mathcal{C}$, leading to a hysteresis in the contact angle. The proposed algorithm is formulated for 3D curved surfaces and it handles varying contact states along $\mathcal{C}$. It is solved within a monolithic finite element formulation. Several examples are shown to demonstrate the performance of the algorithm.

There are several important extensions of the present model that could be considered in future work. One is the modeling of the fluid flow inside the droplet during rolling contact and dynamic impact. The interplay between membrane deformation and fluid flow make this a fluid-structure interaction problem. A second is the consideration of deformable substrates. The challenge there will be to capture the wetting ridge on the substrate. Another extension is the description of coalescing and splitting of droplets. The challenge in that case is the accurate and efficient

modeling of the topology changes associated with coalescing and splitting. In future studies, the presented model can also be used to investigate the wetting behavior of droplets on rough surfaces. Initial work in this direction, considering fixed contact angles, is presented in Osman and Sauer (2014, 2015).

Acknowledgements

The author thanks Dr. Tobias Luginsland and Yannick Omar for proofreading the manuscript.

A Linearization of the FE force vectors

This appendix provides all the FE tangent matrices corresponding to the FE forces given in (55).

A.1 Linearization of $\mathbf{f}^e_{\text{int}}$

Alternatively, expression (55.1) can be written as

$$\mathbf{f}^e_{\text{int}} = \int_{\Omega^e_0} \gamma\, \mathbf{N}^{\mathrm{T}}_{,\alpha}\, a^{\alpha\beta}\, \mathbf{N}_{,\beta}\, J\, \mathrm{d}A\, \mathbf{x}_e \ . \tag{62}$$

With the help of

$$\Delta J = \frac{J}{2}\, a^{\gamma\delta}\, \Delta a_{\gamma\delta} \ , \tag{63}$$

$$\Delta a^{\alpha\beta} = -\frac{1}{2}\big(a^{\alpha\gamma} a^{\beta\delta} + a^{\alpha\delta} a^{\beta\gamma}\big)\, \Delta a_{\gamma\delta} \ , \tag{64}$$

$$\Delta a_{\gamma\delta} = \boldsymbol{a}_\gamma \cdot \Delta \boldsymbol{a}_\delta + \boldsymbol{a}_\delta \cdot \Delta \boldsymbol{a}_\gamma \ , \tag{65}$$

(Sauer and Duong, 2015) and

$$\Delta \boldsymbol{a}_\alpha \approx \mathbf{N}_{,\alpha}\, \Delta \mathbf{x}_e \ , \tag{66}$$

one finds the increment

$$\Delta \mathbf{f}^e_{\text{int}} = \big(\mathbf{k}^e_{\text{geo}} + \mathbf{k}^e_{\text{mat}}\big)\, \Delta \mathbf{x}_e \ , \tag{67}$$

with

$$\mathbf{k}^e_{\text{geo}} = \int_{\Omega^e} \gamma\, \mathbf{N}^{\mathrm{T}}_{,\alpha}\, a^{\alpha\beta}\, \mathbf{N}_{,\beta}\, \mathrm{d}a \ , \tag{68}$$

and

$$\mathbf{k}^e_{\text{mat}} = \int_{\Omega^e} \gamma\, \mathbf{N}^{\mathrm{T}}_{,\alpha} \Big(\boldsymbol{a}^\alpha \otimes \boldsymbol{a}^\beta - \boldsymbol{a}^\beta \otimes \boldsymbol{a}^\alpha - a^{\alpha\beta} \boldsymbol{i}\Big)\, \mathbf{N}_{,\beta}\, \mathrm{d}a \ . \tag{69}$$

Tangent matrix $\mathbf{k}^e_{\text{mat}}$ is equivalent to the less efficient expression given in Sauer (2014). Adding $\mathbf{k}^e_{\text{geo}}$ and $\mathbf{k}^e_{\text{mat}}$ gives

$$\mathbf{k}^e_{\text{int}} = \int_{\Omega^e} \gamma\, \mathbf{N}^{\mathrm{T}}_{,\alpha} \Big(a^{\alpha\beta}\, \boldsymbol{n} \otimes \boldsymbol{n} + \boldsymbol{a}^\alpha \otimes \boldsymbol{a}^\beta - \boldsymbol{a}^\beta \otimes \boldsymbol{a}^\alpha\Big)\, \mathbf{N}_{,\beta}\, \mathrm{d}a \ . \tag{70}$$

A.2 Linearization of $\mathbf{f}^e_{\text{sta}}$

Expression (55.2) can also be written as

$$\mathbf{f}^e_{\text{sta}} = \int_{\Omega^e_0} \tau^{\alpha\beta}_{\text{sta}} \left(\mathbf{N}^{\mathrm{T}}_{,\alpha} \mathbf{N}_{,\beta} + \mathbf{N}^{\mathrm{T}} (\boldsymbol{n} \otimes \boldsymbol{n}) \mathbf{N}_{,\alpha\beta} \right) \mathrm{d}A \, \mathbf{x}_e \ , \tag{71}$$

where $\tau^{\alpha\beta}_{\text{sta}} = J\sigma^{\alpha\beta}_{\text{sta}}$ and $\mathbf{N}_{,\alpha\beta} = \left[N_{1,\alpha\beta}\mathbf{1},\ N_{2,\alpha\beta}\mathbf{1},\ ...,\ N_{n_e,\alpha\beta}\mathbf{1} \right]$. Using

$$\Delta \boldsymbol{n} = -\boldsymbol{a}^{\gamma} (\boldsymbol{n} \cdot \Delta \boldsymbol{a}_{\gamma}) \tag{72}$$

and

$$\Delta \tau^{\alpha\beta}_{\text{sta}} = \frac{\mu}{2} \left(a^{\alpha\gamma} a^{\beta\delta} + a^{\alpha\delta} a^{\beta\gamma} \right) \Delta a_{\gamma\delta} \ , \tag{73}$$

(Sauer, 2014; Sauer and Duong, 2015) along with (65) gives

$$\Delta \mathbf{f}^e_{\text{sta}} = \mathbf{k}^e_{\text{sta}} \, \Delta \mathbf{x}_e \ , \tag{74}$$

with

$$\begin{aligned} \mathbf{k}^e_{\text{sta}} \ = & \int_{\Omega^e_0} \mu \, \mathbf{N}^{\mathrm{T}}_{,\alpha} \left(\boldsymbol{a}^{\beta} \otimes \boldsymbol{a}^{\alpha} + a^{\alpha\beta} \boldsymbol{i} \right) \mathbf{N}_{,\beta} \, \mathrm{d}A + \int_{\Omega^e_0} 2\mu \, b^{\alpha\beta} \, \mathbf{N}^{\mathrm{T}} (\boldsymbol{n} \otimes \boldsymbol{a}_{\alpha}) \, \mathbf{N}_{,\beta} \, \mathrm{d}A \\ & + \int_{\Omega^e_0} \tau^{\alpha\beta}_{\text{sta}} \left(\mathbf{N}^{\mathrm{T}}_{,\alpha} \mathbf{N}_{,\beta} + \mathbf{N}^{\mathrm{T}} (\boldsymbol{n} \otimes \boldsymbol{n}) \, \mathbf{N}_{;\alpha\beta} + b_{\alpha\beta} \, \mathbf{N}^{\mathrm{T}} (\boldsymbol{a}^{\gamma} \otimes \boldsymbol{n}) \, \mathbf{N}_{,\gamma} \right) \mathrm{d}A \ . \end{aligned} \tag{75}$$

Here we have introduced

$$\mathbf{N}_{;\alpha\beta} = \mathbf{N}_{,\alpha\beta} - \Gamma^{\gamma}_{\alpha\beta} \, \mathbf{N}_{,\gamma} \ , \tag{76}$$

with $\Gamma^{\gamma}_{\alpha\beta} := \boldsymbol{a}^{\gamma} \cdot \boldsymbol{a}_{\alpha,\beta}$. Tangent matrix $\mathbf{k}^e_{\text{sta}}$ is also equivalent to the less efficient expression given in Sauer (2014).[6]

A.3 Linearization of $\mathbf{f}^e_{\text{c}}$

For hydrostatic surface contact between the droplet and a motionless substrate, expression (55.3) can be written as

$$\mathbf{f}^e_{\text{c}} = -\int_{\Omega^e_0} \mathbf{N}^{\mathrm{T}} \, \boldsymbol{f}_{\text{c}} \, J \, \mathrm{d}A \ , \tag{77}$$

where

$$\boldsymbol{f}_{\text{c}} = \begin{cases} -\epsilon_{\text{n}} \, g_{\text{n}} \, \boldsymbol{n}_{\text{c}} & \text{if } g_{\text{n}} < 0 \ , \\ \mathbf{0} & \text{if } g_{\text{n}} \geq 0 \ , \end{cases} \tag{78}$$

is the contact traction according to the penalty model (14). Here, $\boldsymbol{n}$ has been replaced by the negative substrate normal $-\boldsymbol{n}_{\text{c}}$. Employing (63) and

$$\Delta \boldsymbol{f}_{\text{c}} = \frac{\partial \boldsymbol{f}_{\text{c}}}{\partial \boldsymbol{x}_{\text{c}}} \, \mathbf{N} \, \Delta \mathbf{x}_e \ , \tag{79}$$

where (Sauer and De Lorenzis, 2013)

$$\frac{\partial \boldsymbol{f}_{\text{c}}}{\partial \boldsymbol{x}_{\text{c}}} = \begin{cases} -\epsilon_{\text{n}} \, \boldsymbol{n}_{\text{c}} \otimes \boldsymbol{n}_{\text{c}} - \epsilon_{\text{n}} \, g_{\text{n}} \dfrac{\partial \boldsymbol{n}_{\text{c}}}{\partial \boldsymbol{x}_{\text{c}}} & \text{if } g_{\text{n}} < 0 \ , \\ \mathbf{0} & \text{if } g_{\text{n}} \geq 0 \ , \end{cases} \tag{80}$$

[6] $\mathbf{k}^e_{\text{sta}} = \mathbf{k}^e_{\text{geo}}\left(\tau^{\alpha\beta}_{\text{sta}}\right) + \mathbf{k}^e_{\text{mat}}\left(\tau^{\alpha\beta}_{\text{sta}}\right) - \mathbf{k}^e_{\text{into}}\left(\tau^{\alpha\beta}_{\text{sta}}\right)$ based on Eqs. (82), (84), (85), (89) and (90) from Sauer (2014).

we find

$$\Delta \mathbf{f}_{\mathrm{c}}^{e} = \mathbf{k}_{\mathrm{c}}^{e}\, \Delta \mathbf{x}_{e} \ , \tag{81}$$

with

$$\mathbf{k}_{\mathrm{c}}^{e} = -\int_{\Omega^e} \mathbf{N}^{\mathrm{T}}\, \frac{\partial \boldsymbol{f}_{\mathrm{c}}}{\partial \boldsymbol{x}_{\mathrm{c}}} \mathbf{N}\, \mathrm{d}a - \int_{\Omega^e} \mathbf{N}^{\mathrm{T}}\, (\boldsymbol{f}_{\mathrm{c}} \otimes \boldsymbol{a}^{\alpha})\, \mathbf{N}_{,\alpha}\, \mathrm{d}a \ . \tag{82}$$

The term $\partial \boldsymbol{n}_{\mathrm{c}} / \partial \boldsymbol{x}_{\mathrm{c}}$ depends on the substrate surface. For flat surfaces it is zero. For the curved surface in Sec. 6.4 it is given in Tab. 2.

A.4 Linearization of $\mathbf{f}_{\boldsymbol{q}_{\mathrm{c}}}^{e}$

The contribution to Eq. (55.5) due to $\boldsymbol{q}_{\mathrm{c}}$ can also be written as

$$\mathbf{f}_{\boldsymbol{q}_{\mathrm{c}}}^{e} = \int_{-1}^{1} \mathbf{N}_{\mathrm{t}}^{\mathrm{T}}\, \boldsymbol{q}_{\mathrm{c}}\, \|\boldsymbol{a}_{\mathrm{c}}\|\, \mathrm{d}\xi \ . \tag{83}$$

This leads to

$$\Delta \mathbf{f}_{\boldsymbol{q}_{\mathrm{c}}}^{e} = \int_{-1}^{1} \mathbf{N}_{\mathrm{t}}^{\mathrm{T}} \left(\Delta \boldsymbol{q}_{\mathrm{c}}\, \|\boldsymbol{a}_{\mathrm{c}}\| + (\boldsymbol{q}_{\mathrm{c}} \otimes \bar{\boldsymbol{a}}_{\mathrm{c}})\, \Delta \boldsymbol{a}_{\mathrm{c}} \right) \mathrm{d}\xi \ , \tag{84}$$

where $\bar{\boldsymbol{a}}_{\mathrm{c}} := \boldsymbol{a}_{\mathrm{c}} / \|\boldsymbol{a}_{\mathrm{c}}\|$ and

$$\Delta \boldsymbol{q}_{\mathrm{c}} = q_{\mathrm{m}}\, \Delta \boldsymbol{m}_{\mathrm{c}} - \gamma_{\mathrm{LG}} \sin\theta_{\mathrm{c}}\, \Delta \boldsymbol{n}_{\mathrm{c}} - \gamma_{\mathrm{LG}} \left(\sin\theta_{\mathrm{c}}\, \boldsymbol{m}_{\mathrm{c}} + \cos\theta_{\mathrm{c}}\, \boldsymbol{n}_{\mathrm{c}} \right) \Delta\theta_{\mathrm{c}} \ , \tag{85}$$

according to (15). The contributions

$$\begin{aligned}
\Delta \boldsymbol{a}_{\mathrm{c}} &= \mathbf{A}_{\mathrm{c}}\, \Delta \mathbf{x}_{e} \ , \qquad \mathbf{A}_{\mathrm{c}} := \mathbf{N}_{\mathrm{t},\xi} \ , \\
\Delta \boldsymbol{n}_{\mathrm{c}} &= \mathbf{N}_{\mathrm{c}}\, \Delta \mathbf{x}_{e} \ , \qquad \mathbf{N}_{\mathrm{c}} := \frac{\partial \boldsymbol{n}_{\mathrm{c}}}{\partial \boldsymbol{x}_{\mathrm{c}}}\, \mathbf{N}_{\mathrm{t}} \ , \\
\Delta \boldsymbol{m}_{\mathrm{c}} &= \mathbf{M}_{\mathrm{c}}\, \Delta \mathbf{x}_{e} \ , \qquad \mathbf{M}_{\mathrm{c}} := -(\boldsymbol{a}^{\mathrm{c}} \otimes \boldsymbol{m}_{\mathrm{c}})\, \mathbf{A}_{\mathrm{c}} - (\boldsymbol{n}^{\mathrm{c}} \otimes \boldsymbol{m}_{\mathrm{c}})\, \mathbf{N}_{\mathrm{c}} \ ,
\end{aligned} \tag{86}$$

have already been obtained in Sauer (2014), where θ_{c} was considered fixed and consequently $\Delta\theta_{\mathrm{c}}$ was not needed. Now $\Delta\theta_{\mathrm{c}}$ needs to be accounted for. For sliding $\Delta\theta_{\mathrm{c}} = 0$, while for sticking

$$\Delta\theta_{\mathrm{c}} = \frac{\epsilon_{\mathrm{t}}}{\gamma_{\mathrm{LG}}\, \sin\theta_{\mathrm{c}}} \left[(\boldsymbol{x}_{\mathrm{c}} - \boldsymbol{x}_{\mathrm{m}}(\boldsymbol{\xi}_{\mathrm{s}}^{n})) \cdot \Delta \boldsymbol{m}_{\mathrm{c}} + \boldsymbol{m}_{\mathrm{c}} \cdot (\Delta \boldsymbol{x}_{\mathrm{c}} - \Delta \boldsymbol{x}_{\mathrm{m}}(\boldsymbol{\xi}_{\mathrm{s}}^{n})) \right] \ , \tag{87}$$

according to Tab. 1. Here the superscript $n+1$ has been skipped. It applies to all quanities apart from $\boldsymbol{\xi}_{\mathrm{s}}^{n}$. Since the substrate surface is not considered to deform here, $\Delta \boldsymbol{x}_{\mathrm{m}} = \mathbf{0}$. Therefore

$$\Delta\theta_{\mathrm{c}} = \frac{\epsilon_{\mathrm{t}}}{\gamma_{\mathrm{LG}}\, \sin\theta_{\mathrm{c}}} \left[(\boldsymbol{x}_{\mathrm{c}} - \boldsymbol{x}_{\mathrm{m}}(\boldsymbol{\xi}_{\mathrm{s}}^{n})) \cdot \mathbf{M}_{\mathrm{c}} + \boldsymbol{m}_{\mathrm{c}} \cdot \mathbf{N}_{\mathrm{t}} \right] \Delta \mathbf{x}_{e} \ . \tag{88}$$

From this follows

$$\Delta \boldsymbol{q}_{\mathrm{c}} = \mathbf{Q}_{\mathrm{c}}\, \Delta \mathbf{x}_{e} \ , \tag{89}$$

with

$$\begin{aligned}
\mathbf{Q}_{\mathrm{c}} := {} & \left[q_{\mathrm{m}}\, \mathbf{1} - \epsilon_{\mathrm{t}} \left(\boldsymbol{m}_{\mathrm{c}} + \cot\theta_{\mathrm{c}}\, \boldsymbol{n}_{\mathrm{c}} \right) \otimes \left(\boldsymbol{x}_{\mathrm{c}} - \boldsymbol{x}_{\mathrm{m}}(\boldsymbol{\xi}_{\mathrm{c}}^{n}) \right) \right] \mathbf{M}_{\mathrm{c}} \\
& - \gamma_{\mathrm{LG}}\, \sin\theta_{\mathrm{c}}\, \mathbf{N}_{\mathrm{c}} - \epsilon_{\mathrm{t}} \left(\left(\boldsymbol{m}_{\mathrm{c}} + \cot\theta_{\mathrm{c}}\, \boldsymbol{n}_{\mathrm{c}} \right) \otimes \boldsymbol{m}_{\mathrm{c}} \right) \mathbf{N}_{\mathrm{t}} \ .
\end{aligned} \tag{90}$$

Writing

$$\Delta \mathbf{f}_{\boldsymbol{q}_{\mathrm{c}}}^{e} = \mathbf{k}_{\boldsymbol{q}_{\mathrm{c}}}^{e}\, \Delta \mathbf{x}_{e} \ , \tag{91}$$

reveals the tangent

$$\mathbf{k}_{\boldsymbol{q}_{\mathrm{c}}}^{e} = \int_{-1}^{1} \mathbf{N}_{\mathrm{t}}^{\mathrm{T}} \left(\mathbf{Q}_{\mathrm{c}}\, \|\boldsymbol{a}_{\mathrm{c}}\| + (\boldsymbol{q}_{\mathrm{c}} \otimes \bar{\boldsymbol{a}}_{\mathrm{c}})\, \mathbf{N}_{\mathrm{t},\xi} \right) \mathrm{d}\xi \ . \tag{92}$$

This expression simplifies to the tangent of Sauer (2014) for the special case $\epsilon_{\mathrm{t}} = 0$. As before, the term $\partial \boldsymbol{n}_{\mathrm{c}} / \partial \boldsymbol{x}_{\mathrm{c}}$ depends on the substrate surface. For flat surfaces it is zero. For the curved surface in Sec. 6.4 it is given in Tab. 2.

A.5 Linearization of $\mathbf{f}_{\bar{p}}^e$

For the examples in Secs. 6.3 and 6.4, the FE force vector

$$\mathbf{f}_{\bar{p}}^e = -\int_{\Omega^e} \mathbf{N}^{\mathrm{T}}\, \bar{p}\, \boldsymbol{n}\, \mathrm{d}a \ , \tag{93}$$

corresponding to the external pressure loading given in Eq. (60), has to be included in Eq. (55.5). From (72) follows

$$\Delta\bar{p} = -\frac{c}{\Delta t}\boldsymbol{n}\cdot\mathbf{N}^*\,\Delta\mathbf{x}_e \ , \tag{94}$$

with

$$\mathbf{N}^* := \mathbf{N} - \boldsymbol{a}^\alpha\cdot\mathbf{N}\left(\mathbf{x}_e - \mathbf{x}_e^{\mathrm{pre}}\right)\mathbf{N}_{,\alpha}\,. \tag{95}$$

Following Sauer et al. (2014), the increment of $\mathbf{f}_{\bar{p}}^e$ can thus be written as

$$\Delta\mathbf{f}_{\bar{p}}^e = \mathbf{k}_{\bar{p}}^e\,\Delta\mathbf{x}_e \ , \tag{96}$$

with

$$\mathbf{k}_{\bar{p}}^e = -\frac{c}{\Delta t}\int_{\Omega^e}\mathbf{N}^{\mathrm{T}}\left(\boldsymbol{n}\otimes\boldsymbol{n}\right)\mathbf{N}^*\,\mathrm{d}a + \int_{\Omega^e}\bar{p}\,\mathbf{N}^{\mathrm{T}}\left(\boldsymbol{n}\otimes\boldsymbol{a}^\alpha - \boldsymbol{a}^\alpha\otimes\boldsymbol{n}\right)\mathbf{N}_{,\alpha}\,\mathrm{d}a \ . \tag{97}$$

References

Berim, G. O. and Ruckenstein, E. (2008). Microscopic calculation of the sticking force for nanodrops on an inclined surface. *J. Chem. Phys.*, **129**(11):114709.

Brakke, K. A. (1992). The surface evolver. *Experimental Mathematics*, **1**(2):141–165.

Brown, R. A., Orr, F. M., and Scriven, L. E. (1980). Static drop on an inclined plate: Analysis by the finite element method. *J. Colloid Interface Sci.*, **73**(1):76–87.

Chou, T.-H., Hong, S.-J., Sheng, Y.-J., and Tsao, H.-K. (2012). Drops sitting on a tilted plate: Receding and advancing pinning. *Langmuir*, **28**:5158–5166.

Das, A. K. and Das, P. K. (2009). Simulation of drop movement over an inclined surface using smoothed particle hydrodynamics. *Langmuir*, **25**(19):11459–11466.

Dimitrakopoulos, P. and Higdon, J. J. L. (1999). On the gravitational displacement of three-dimensional fluid droplets from inclined solid surfaces. *J. Fluid Mech.*, **395**:181–209.

Dong, S. (2012). On imposing dynamic contact-angle boundary conditions for wall-bounded liquid-gas flows. *Comput. Methods Appl. Mech. Engrg.*, **247-248**:179–200.

Dupuis, A. and Yeomans, J. M. (2006). Dynamics of sliding drops on superhydrophobic surfaces. *Europhys. Lett.*, **75**(1):105–111.

Dussan V., E. B. (1979). On the spreading of liquids on solid surfaces: Static and dynamic contact lines. *Ann. Rev. Fluid Mech.*, **11**:371–400.

Dussan V., E. B. and Chow, R. T. P. (1983). On the ability of drops or bubbles to stick to non-horizontal surfaces of solids. *J. Fluid Mech.*, **137**:1–29.

ElSherbini, A. I. and Jacobi, A. M. (2004). Liquid drops on vertical and inclined surfaces II. A method for approximating drop shapes. *J. Colloid Interface Sci.*, **273**:566–575.

Extrand, C. W. and Kumagai, Y. (1995). Liquid-drops on an inclined plane - the relation between contact angles, drop shape, and retentive force. *J. Colloid Interface Sci.*, **170**(2):515–521.

Fang, C., Hidrovo, C., Wang, F., Eaton, J., and Goodson, K. (2008). 3-D numerical simulation of contact angle hysteresis for microscale two phase flow. *Int. J. Multiphase Flow*, **34**:690–705.

Goyal, S., Ruina, A., and Papadopoulos, J. (1991). Planar sliding with dry friction. Part 1. Limit surface and moment function. *Wear*, **143**:307–330.

Iliev, S. D. (1995). Iterative method for the shape of static drops. *Computer Methods in Applied Mechanics and Engineering*, **126**:251–265.

Iliev, S. D. and Pesheva, N. (2006). Nonaxisymmetric drop shape analysis and its application for determination of the local contact angles. *J. Colloid Interface Sci.*, **301**(3-4):677–684.

Janardan, N. and Panchagnula, M. V. (2014). Effect of the initial conditions on the onset of motion in sessile drops on tilted plates. *Colloid. Surf. A*, **456**:238–245.

Laursen, T. A. (2002). *Computational Contact and Impact Mechanics: Fundamentals of modeling interfacial phenomena in nonlinear finite element analysis*. Springer.

Lawal, A. and Brown, R. A. (1982a). The stability of an inclined pendent drop. *J. Colloid Interface Sci.*, **89**(2):332–345.

Lawal, A. and Brown, R. A. (1982b). The stability of inclined sessile drops. *J. Colloid Interface Sci.*, **89**(2):346–352.

Milinazzo, F. and Shinbrot, M. (1988). A numerical study of a drop on a vertical wall. *J. Colloid Interface Sci.*, **121**(1):254–264.

Minaki, H. and Li, S. (2014). Multiscale modeling and simulation of dynamic wetting. *Comp. Meth. Appl. Mech. Engrg.*, **273**:273–302.

Osman, M. and Sauer, R. A. (2014). A parametric study of the hydrophobicity of rough surfaces based on finite element computations. *Colloid Surface A*, **461**:119–125.

Osman, M. and Sauer, R. A. (2015). Computational analysis of wetting on hydrophobic surfaces: Application to self-cleaning mechanisms. In Mittal, K. L., editor, *Advances in Contact Angle, Wettability and Adhesion, Volume 2*. Wiley.

Park, Y.-G. and Jacobi, M. (2009). Numerical modeling of liquid drop spreading behavior on inclined surfaces. In *Proceedings of ASME 2009 Heat Transfer Summer Conference*, volume 3, pages 367–373. ASME.

Prabhala, B. R., Panchagnula, M. V., and Vedantam, S. (2013). Three-dimensional equilibrium shapes of drops on hysteretic surfaces. *Colloid. Polym. Sci.*, **291**:279–289.

Rotenberg, Y., Borkuvka, L., and Neumann, A. W. (1984). The shape of nonaxisymmetric drops on inclined planar surfaces. *J. Colloid Interface Sci.*, **102**(2):424–434.

Santos, M. J. and White, J. A. (2011). Theory and simulation of angular hysteresis on planar surfaces. *Langmuir*, **27**:14868–14875.

Sauer, R. A. (2014). Stabilized finite element formulations for liquid membranes and their application to droplet contact. *Int. J. Numer. Meth. Fluids*, **75**(7):519–545.

Sauer, R. A. (2016). A contact theory for surface tension driven systems. *Math. Mech. Solids*, **21**(3):305–325.

Sauer, R. A. and De Lorenzis, L. (2013). A computational contact formulation based on surface potentials. *Comput. Methods Appl. Mech. Engrg.*, **253**:369–395.

Sauer, R. A. and De Lorenzis, L. (2015). An unbiased computational contact formulation for 3D friction. *Int. J. Numer. Meth. Engrg.*, **101**(4):251–280.

Sauer, R. A. and Duong, T. X. (2015). On the theoretical foundations of solid and liquid shells. *Math. Mech. Solids*, published online, DOI: 10.1177/1081286515594656.

Sauer, R. A., Duong, T. X., and Corbett, C. J. (2014). A computational formulation for constrained solid and liquid membranes considering isogeometric finite elements. *Comput. Methods Appl. Mech. Engrg.*, **271**:48–68.

Sauer, R. A., Duong, T. X., Mandadapu, K. K., and Steigmann, D. J. (2016). A stabilized finite element formulation for liquid shells and its application to lipid bilayers. *J. Comput. Phys.*, published online, DOI: 10.1016/j.jcp.2016.11.004.

Schwartz, L. W., Roux, D., and Cooper-White, J. J. (2005). On the shapes of droplets that are sliding on a vertical wall. *Physica D*, **209**:236–244.

Semprebon, C. and Brinkmann, M. (2014). On the onset of motion of sliding drops. *Soft Matter*, **10**(18):3325–3334.

Sethian, J. A. and Smerekar, P. (2003). Level set methods for fluid interfaces. *Annu. Rev. Fluid Mech.*, **35**:341–372.

Steigmann, D. J. (1999). Fluid films with curvature elasticity. *Arch. Rat. Mech. Anal.*, **150**:127–152.

Steigmann, D. J. and Li, D. (1995). Energy-minimizing states of capillary systems with bulk, surface and line phases. *IMA J. Appl. Math.*, **55**(1):1–17.

Sui, Y., Ding, H., and Spelt, P. D. M. (2014). Numerical simulations of flows with moving contact lines. *Annu. Rev. Fluid Mech.*, **46**:97–119.

Tadmor, R. (2011). Approaches in wetting phenomena. *Soft Matter*, **7**:1577–1580.

Thampi, S. P., Adhikari, R., and Govindarajan, R. (2013). Do liquid drops roll or slide on inclined surfaces? *Langmuir*, **29**(10):3339–3346.

Thompson, P. A. and Robbins, M. O. (1989). Simulations of contact-line motion: Slip and the dynamic contact angle. *Phys. Rev. Let.*, **7**:766–769.

Wriggers, P. (2006). *Computational Contact Mechanics*. Springer, 2$^{\text{nd}}$ edition.